Local wave-activity analysis of atmospheric blocks in the Northern Hemisphere winter

Pragallva Barpanda[a] , Noboru Nakamura[b] ,

[a] *Geophysical Institute, University of Bergen and Bjerknes Center for Climate Research, Norway*

[b] *Department of the Geophysical Sciences, The University of Chicago, Chicago, USA*

Pragallva Barpanda's old affiliation: Department of the Geophysical Sciences, The University of Chicago, Chicago, Illinois

Corresponding author: Pragallva Barpanda, pragallva.barpanda@uib.no

ABSTRACT: Atmospheric blocking entails a persistent, anomalous meandering of the jet stream that disrupts the eastward migration of transient eddies in the midlatitudes. Here we analyze a large number of blocking (and blocking-like) events in the Northern Hemisphere winter with the ERA5 reanalysis through the lens of vertically-averaged wave-activity budget. By applying a feature tracking algorithm, large-valued wave-activity anomalies that persist for 4 days or longer at a given location are identified as blocks, and block-centered composites are constructed for the wave-activity budget through the lifecycle of blocks. The identified events share commonly recognized features of blocking. The majority of the persistent events occur in clusters collocated with the quasi-stationary ridge associated with the Atlantic and the Pacific storm track. Frequency of persistent blocks is higher (lower) in regions where the 'carrying capacity' of the jet stream is lower (higher). A very low carrying capacity for the transient waves leads to a large population of blocks over Europe. The composite lifecycle of persistent blocks shows that convergence (divergence) of the zonal flux of wave-activity dominates the budget during the onset (decay) phase of the block, while the eddy-induced wind plays a crucial role of suppressing the zonal flux during the maturation period. Our finding broadly supports the 'traffic jam' hypothesis of Nakamura and Huang as a common mechanism of block formation, although there is vast diversity in the actual manifestation of individual blocks.

SIGNIFICANCE STATEMENT: The purpose of this study is to better understand why the eastward progression of weather systems occasionally stalls in the midlatitudes resulting in a peculiar phenomenon known as atmospheric blocking. Blocking is one of the leading causes of extreme weather in the midlatitudes yet its prediction often proves challenging. Our results identify the common dynamical processes that define the blocking lifecycle during the Northern Hemisphere winter. Particularly, blocks are shown to be a result of self-induced flow deceleration that occurs when the midlatitude waves grow very large in amplitude. Using a newly developed block detection algorithm, the study draws an insightful analogy between blocking and traffic congestion on a highway, suggesting that blocking is more prevalent in regions where the jet stream's 'carrying capacity' is lower and less frequent in regions where it is higher.

1. Introduction

Atmospheric blocking is a type of anomalous weather event in the midlatitudes that disrupts the typical eastward migration of high/low pressure systems (Rossby waves) due to persistent meandering of the jet stream (Rex 1950; Berggren et al. 1949; Woollings et al. 2010b, 2018). Atmospheric blocks usually manifest as a quasi-stationary cyclone/anticyclone that can persist at a location from a few days to more than a week and often results in unusually high/low temperatures, drought/deluge, and other forms of weather anomalies depending on the location and season of occurence (Demirtaş 2017; Lupo 2021; Kautz et al. 2022). These systems often emerge spontaneously without a well-defined precursor, thus making them a leading cause of 'forecast busts' in the midlatitudes (Rodwell et al. 2013).

Given that blocking was recognized more than seven decades ago (Rex 1950; Berggren et al. 1949), and given the abundance of meteorological data and computational resources today, it is somewhat surprising that we still do not have a prevailing theory for blocking in a manner similar to baroclinic instability (Charney 1947; Eady 1949; Phillips 1951), stratospheric wave-mean flow interaction (Charney and Drazin 1961; Lindzen and Holton 1968; Matsuno 1971; Andrews and McIntyre 1976; Plumb 1977) or the meridional overturning circulation (Eliassen 1952; Kuo 1956; Held and Hou 1980; Johnson 1989).

Early attempts to explain blocking as a resonant amplification of a stationary planetary wave by an external forcing (Tung and Lindzen 1979; Charney and DeVore 1979) resurfaced in recent years with a renewed interest in the Northern Hemisphere summer blocking and associated heat waves (Petoukhov et al. 2013; Mann et al. 2018). The resonance theory requires a Rossby wave train to be guided over topography and other external forcing for a sufficiently long time; whether this condition is met in the atmosphere is still under debate (Wirth and Polster 2022). During the 1980s, modons and other solitary waves were recognized as a possible unforced solution of the nonlinear governing equations and considered a prototype of blocking (e.g. McWilliams 1980; Butchart et al. 1989; Haines and Marshall 1987). Yet it remains unclear what processes lead to the creation of the solitary feature from a wavy flow. A widely recognized eddy straining mechanism (Shutts 1983) offers an explanation for the maintenance of a pre-existing block but it does not address blocking onset [see a related discussion on selective absorption mechanism by Yamazaki and Itoh (2013)]. There is also a body of literature that treats blocking as an emergent coherent structure in a high-dimensional, chaotic dynamical system rather than as a local wave phenomenon (Legras and Ghil 1985; Ghil et al. 2019; Lucarini and Gritsun 2019).

Despite the disparate theoretical characterizations of blocking, there is sufficient evidence to suggest that the interaction between transient eddies and background diffluent flow plays an important role in shaping blocking episodes (Berggren et al. 1949; Green 1977; Shutts 1983; Colucci 2001; Trenberth 1986; Mullen 1987; Nakamura et al. 1997; Pelly and Hoskins 2003; Woollings et al. 2008; Altenhoff et al. 2008). Some conceptual models based on the interaction of waves and flows over different scales show promise (Luo 2005; Luo et al. 2019; Swanson 2000), although they are not readily verifiable using observed blocking episodes. Meanwhile, there has been a growing attention to the role of diabatic heating associated with moist processes (Pfahl et al. 2015; Steinfeld and Pfahl 2019). A moist blocking theory remains largely unexplored.

In recent years, the *finite-amplitude local wave-activity* (LWA) theory has emerged as a viable framework to address atmospheric blocking because it allows a description of large-amplitude Rossby waves including wave-breaking features, which are typically associated with atmospheric blocks. First proposed by Huang and Nakamura (2016, 2017), LWA measures Rossby wave amplitude using the meridional displacement of quasigeostrophic potential vorticity (QGPV) from a 'zonalized' reference state (Huang and Nakamura 2016, see their Fig.1). In addition, LWA vastly improves the budget from its small-amplitude limit and affords a relatively simple interpretation for the role of wave-activity fluxes and other physical processes responsible for the growth of anomalously large wave events (Nakamura 2024). For example, Neal et al. (2022) use the LWA budget to quantify the effects of diabatic heating from an upstream cyclone on the blocking anticyclone that drove the 2021 Pacific Northwest heatwave.

Based on the observed budget of vertically-averaged LWA, Nakamura and Huang (2018, hereafter NH18) proposed a semi-empirical theory for atmospheric blocking. In their conceptual model, the wave-activity budget along the jet stream is reduced to a 1-dimensional nonlinear partial differential equation which mathematically appears similar to the well-studied Lighthill–Whitham–Richards model for a traffic flow (Lighthill and Whitham 1955; Richards 1956). Just as an increased traffic density slows down the traffic speed on a highway, an increased LWA slows down the westerly wind of the jet stream. This causes the eastward wave-activity flux (zonal LWA flux) to reach a maximum ('carrying capacity' of the jet stream) at a threshold value of wave-activity, beyond which the stalling of the westerly wind proceeds spontaneously. NH18 dubbed this process the traffic jam mechanism for the onset of atmospheric blocking.

The 1D traffic-flow model has been used for examining the connection between dynamics and statistics of blocking in hypothetical climate scenarios. Paradise et al. (2019) and Valva and Nakamura (2021) integrated the model with prescribed (pseudostochastic) eddy forcing and showed that the blocking statistics are modulated by the stationary wave amplitude, jet speed and amplitude of transient forcings. Using an idealized numerical model, Nakamura and Huang (2017) demonstrate that the traffic-jam mechanism is also plausible in 2D flows representative of a jet stream along a potential vorticity front. Recently, Polster and Wirth (2023) tested the traffic jam idea in the context of ensemble reforecast of an observed blocking event over the North Atlantic. They find the mechanism relevant for the particular event examined.

In the present work, we investigate a large number of observed blocking events for the Northern Hemisphere (NH) winter using ERA5 reanalysis (1979-2022). Using the vertically-averaged budget of wave-activity, we aim to identify common dynamics that underlies diverse manifestations of blocking events. To this end, we employ a feature-tracking algorithm to identify all large-amplitude Rossby waves that appear as persistent anomalies in the NH jet stream and classify them into cyclonic/anticyclonic events. We then conduct block-centered composite analyses of the LWA budget throughout their life cycle. Attention is paid to the role of the zonal flux of wave-activity and its modification by the eddy-induced flow, a key aspect of the traffic jam theory. Furthermore, we evaluate the utility of the carrying capacity as a predictor for the block statistics. We restrict our attention to the NH winter. Comparisons with summertime and the Southern Hemisphere (SH) atmospheric blocks are deferred to a future study.

The paper is organized as follows. In section 2, we review the LWA framework and the theory behind the traffic jam mechanism. In section 3, we describe the feature-tracking algorithm used for identifying major persistent anomalies in the jet stream. Section 4 presents the spatial distribution, life cycle, and the LWA budget analysis of all the tracked events. Finally, we conclude and summarize our results in section 5.

2. Brief review of LWA framework

a. Wave-activity and its budget

We use the local wave-activity (LWA) framework to study atmospheric blocks. LWA ($\mathcal{A}$) measures the amplitude of the Rossby wave by the meridional displacement of QGPV (q) from a zonally symmetric reference state $\left(q_{REF}\right)$. In the spherical coordinate, LWA is expressed as

$$\mathcal{A}(\lambda, \phi, z, t)\ \cos\phi \quad = \quad -a \int_{0}^{\Delta\phi} \left(q - q_{REF}\right) \cos(\phi + \hat{\phi}) d\hat{\phi}, \tag{1}$$

where a is the radius of the Earth, (λ, ϕ, z, t) denote longitude, latitude, pressure pseudo-height and time, respectively. $\hat{\phi}$ is a displacement coordinate and $\hat{\phi} = \Delta\phi\,(\lambda, \phi, z, t)$ defines the instantaneous meridional displacement of a QGPV contour with respect to the latitude circle, ϕ. In this framework, the wave-free reference state $q_{REF}(\phi, z, t)$ is determined by zonalizing QGPV contours (Huang and Nakamura 2016). The reference-state zonal winds (u_{REF}) and potential temperature (θ_{REF}) are inverted from q_{REF} with the appropriate boundary conditions (see Neal et al. 2022 and Nakmaura 2024; their supplementary materials). All "eddies" (subsequently denoted with a subscript e) are defined as deviations from the reference state.

The vertically averaged LWA follows the budget given by (Nakamura 2024)

$$\underbrace{\frac{\partial}{\partial t}\langle\mathcal{A}\rangle\cos\phi}_{\text{LWA tendency}} = \underbrace{-\frac{1}{a\cos\phi}\frac{\partial\langle F_\lambda\rangle}{\partial\lambda}}_{\text{(I)}} \underbrace{-\frac{1}{a\cos\phi}\frac{\partial\langle F_\phi\cos\phi\rangle}{\partial\phi}}_{\text{(II)}} \underbrace{-\left\langle e^{z/H}\frac{\partial F_z}{\partial z}\right\rangle}_{\text{(III)}} + \underbrace{\text{residual}}_{\text{(IV)}} \tag{2a}$$

$$\text{where, } F_\lambda = \underbrace{(F_1+F_3)}_{\text{linear}} + \underbrace{(F_2)}_{\text{nonlinear}} \tag{2b}$$

where $\langle\ldots\rangle$ denotes density-weighted vertical average, $H \equiv 7$ km is the assumed scale-height and F_λ, F_ϕ, F_z are the zonal, meridional and vertical wave-activity fluxes, respectively. In addition, F_1 represents the zonal advective flux of LWA by the reference-state wind, F_3 is the radiation stress of Rossby waves and F_2 represents the zonal advective flux by the eddy-induced wind. The exact expressions for the fluxes are given in the second column of Table 1. Terms (I)-(II) in Eq. (2a) are evaluated by performing density-weighted vertical averaging on F_λ and F_ϕ. Term (III) amounts to the injection of F_z at the surface which is a function of meridional eddy heat flux given by $(f\cos\phi/H)\,(v_e\theta_e/S_\theta)_{z=0}$, where v_e and θ_e are eddies of meridional wind and potential temperature, respectively (see Table 1 for the exact expressions of F_λ, F_ϕ and F_z). Here f is the Coriolis parameter and S_θ is the area-weighted hemispheric mean static-stability (Table 1). Finally, Term (IV) is estimated as the residual of the LWA budget. This term may arise due to nonadiabatic and nonquasigeostrophic sources and sinks of LWA tendency, which includes the effects of friction, small-scale turbulence, latent heating and radiative process. When applied to data, the residual of the budget [Term (IV)] inevitably absorbs the analysis errors of the other terms. However, the peak magnitude of the residual is typically comparable to that of the other terms. It suggests that, to the extent that the other terms are analyzed accurately, the residual term holds a comparable accuracy where its values are large.

Note that LWA contains both amplitude and phase information of Rossby waves and geostrophic eddies. After a suitable phase averaging, the fluxes $\vec{\mathcal{F}} = (F_3, F_\phi, F_z)$ will become the zonal, meridional and vertical Eliassen-Palm (EP) fluxes. In the limit of small-amplitude WKB approximation, the vector $\vec{c_g} = \vec{\mathcal{F}}/(\mathcal{A}\cos\phi)$ gives the group velocity of the Rossby waves. Thus Eq. (6) is an extension of the previous linear wave-activity diagnostics [e.g Plumb 1986, his Eq. (2.14)]. In the present study, we apply weak time filtering (4-day low-pass filter) and spatial filtering (15°

Flux	Exact expression	Approx. relation with $\langle\mathcal{A}\rangle$	Description
F_λ	$F_1+F_2+F_3$	$\left(u_0-\alpha\langle\mathcal{A}\rangle+c_g^x\right)\langle\mathcal{A}\rangle\cos\phi$	Total zonal flux
F_1	$u_{REF}\mathcal{A}\cos\phi$	$u_0\langle\mathcal{A}\rangle\cos\phi$	Zonal advective flux of LWA due to reference state wind
F_2	$-a\int_0^{\hat{\phi}} u_e q_e \cos(\phi+\hat{\phi})\, d\hat{\phi}$	$-\alpha\langle\mathcal{A}\rangle^2\cos\phi$	Zonal nonlinear advective flux of LWA
F_3	$\frac{1}{2}\left(v_e^2-u_e^2-\theta_e^2\,\frac{Re^{-\kappa z/H}}{H\,S_\theta}\right)\cos\phi$	$c_g^x\langle\mathcal{A}\rangle\cos\phi$	Zonal radiation stress
F_ϕ	$-(u_e v_e)\cos\phi$	$c_g^y\langle\mathcal{A}\rangle\cos\phi$	Meridional radiation stress
F_z	$(v_e\theta_e)\,\frac{e^{-z/H} f\cos\phi}{S_\theta}$	$c_g^z\langle\mathcal{A}\rangle\cos\phi$	Vertical radiation stress

TABLE 1. A summary of LWA fluxes and their decomposition where $\kappa = R/c_p$, R is the ideal gas constant, c_p is the specific heat at constant pressure of dry air, S_θ is the hemispheric-mean static stability given by $\partial_z\tilde{\theta}$, the three-dimensional group velocity of Rossby waves is given by (c_g^x, c_g^y, c_g^z), the variable u_0 is time- and vertically averaged u_{REF} and the rest of the parameters are defined in the main text.

running-mean along longitude) to smooth out phase variation associated with synoptic transient eddies.

From here onward, the study will focus only on the vertically averaged quantities and the angle brackets will be dropped for simplicity. Additionally, all references to wave-activity in this paper will solely refer to LWA unless otherwise stated.

b. Role of zonal advection and eddy-wind covariance

NH18 introduced additional simplifying approximations to Eq. (2a) based on the observed wave-activity budget: (i) On synoptic timescales, the growth and decay of wave-activity is dominated by the zonal-flux convergence term, i.e, Term (I) dominates the LWA tendency of Eq. (2a) in the storm track region and (ii) locally, the zonal wind covaries negatively with the LWA throughout the storm track region. Both approximations will be scrutinized and their relevance for blocking will be discussed in more detail in the sections below.

To test the first approximation, one can derive a variance budget for wave-activity by time-integrating the LWA tendency term and the RHS terms from Eq. (2a) as,

$$\underbrace{\mathrm{Var}(\mathcal{A}')}_{\text{LWA variance}} = \underbrace{\mathrm{Cov}(\mathcal{A}',\mathrm{I}')}_{\text{(i)}} + \underbrace{\mathrm{Cov}(\mathcal{A}',\mathrm{II}')}_{\text{(ii)}} + \underbrace{\mathrm{Cov}(A',\mathrm{III}')}_{\text{(iii)}} + \underbrace{\mathrm{Cov}\,(\mathcal{A}',\mathrm{IV}')}_{\text{(iv)}}, \tag{3a}$$

$$\text{where } \mathrm{Var}(\mathcal{A}') = \left(\int_t^{t+4} (\partial_{\hat{t}}\mathcal{A}')\, d\hat{t}\right)\left(\int_t^{t+4} (\partial_{\hat{t}}\mathcal{A}')\, d\hat{t}\right)^T \cos\phi \tag{3b}$$

$$\text{and } \mathrm{Cov}\,(\mathcal{A}',\mathrm{X}') = \left(\int_t^{t+4} (\partial_{\hat{t}}\mathcal{A}')\, d\hat{t}\right)\left(\int_t^{t+4} \mathrm{X}' d\hat{t}\right)^T. \tag{3c}$$

Here the prime denotes transient component and the variance is calculated as the change over 4 days. The parentheses in Eqs. (3b) and (3c) are a row matrix consisting of a series of time integrals over consecutive 4-day periods within DJF from 1979-2022, $\hat{t}$ is time in days, T indicates matrix transpose, and X in Eq. (3c) denotes Terms (I)-(IV) in Eq. (2a). All calculations are performed on daily-averaged time series obtained from 6-hourly datasets of LWA and its fluxes. The method used to evaluate transient component (e.g. $\mathcal{A}'$ and X') is described in more detail in the methods section (see section 3a).

Figure 1 maps the terms in Eq. (3a) for DJF 1979-2022. Panels (a) and (b) in Fig. 1 show that the variance of the 4-day change in LWA is largely explained by the covariance with Term (I) in the midlatitudes thus satisfying the first approximation. This is particularly true along the Atlantic storm track region and in the western Pacific. The roles of the other terms are of secondary importance on this timescale, although Term (II) has significant negative contributions east of Japan (Fig. 1c), and Term (IV) contributes positively over the Bay of Alaska and northeast Canada (Fig. 1e). It may appear surprising that the contribution of the surface baroclinic injection (Term III) is very small (Fig. 1d). This is a result of local covariance and does not imply an absence of surface injection: since air is advected downstream, the injection of wave-activity does not necessarily correlate with the *local* tendency of wave-activity. See appendix A for further decomposition of the zonal LWA flux into linear and nonlinear components.

The second approximation, namely, the negative covariance between LWA and zonal wind is introduced semi-empirically in NH18 (see their Fig. 1). This may be expected from the nonacceleration theorem although the local application of this theorem proves unwieldy except for

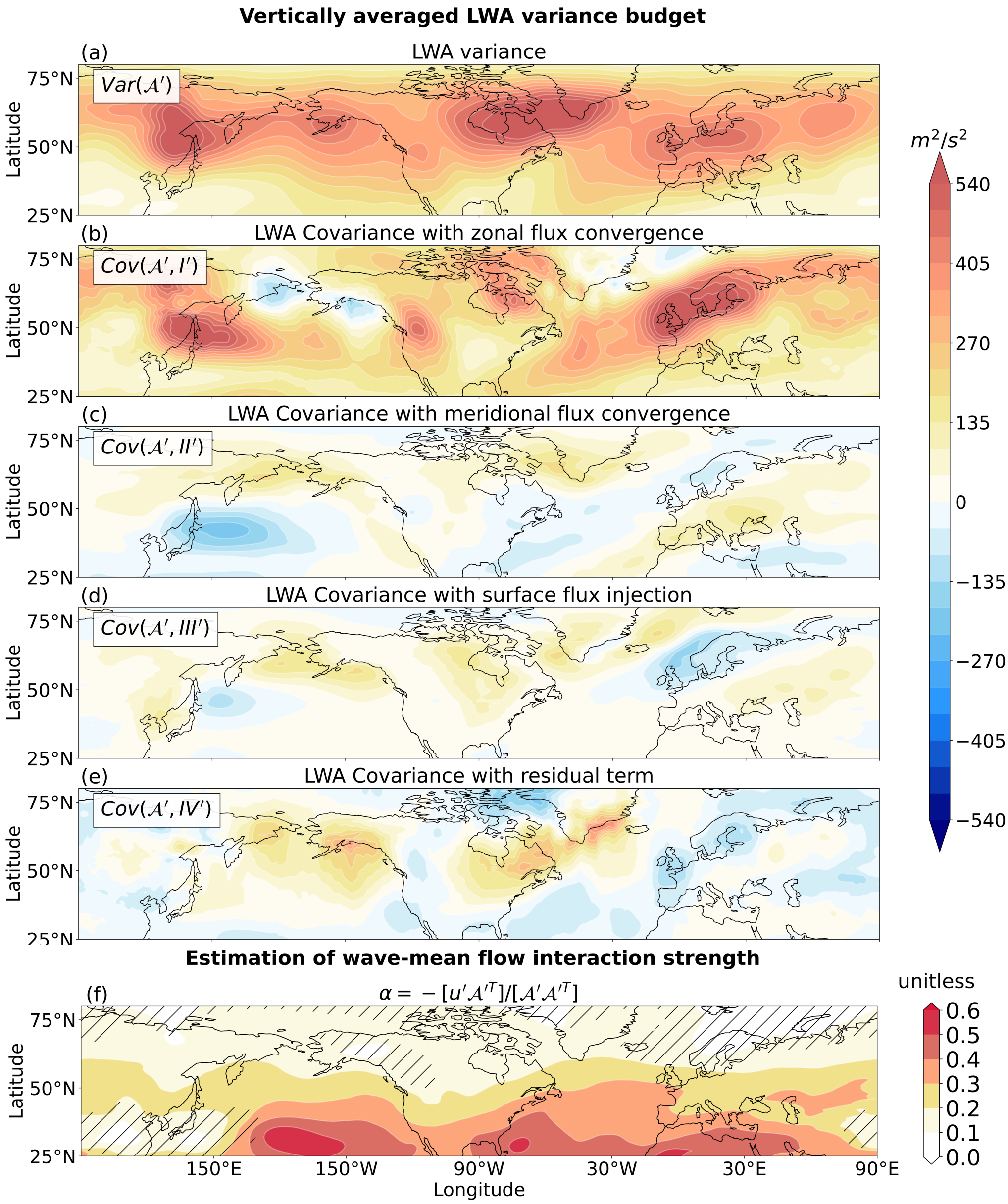

FIG. 1. (a) 4-day variance of the vertically-averaged LWA and its covariance with the 4-day integrated (b) zonal flux convergence, (c) meridional flux convergence, (d) surface flux injection and the (e) residual term. Every panel from (a) through (e) corresponds to each of the terms in Eq. (3a) of the main text. (f) Empirical estimation of α during the same period as above. The stipples in (f) denote regions where the transient zonal wind and wave-activity are weakly correlated, i.e. where the r-value $< |0.5|$ in the estimation of α. All panels show averaged values over DJF during 1979-2022 from ERA5 dataset.

certain limiting cases (Huang and Nakamura 2016). Nevertheless, the negative covariance between the vertically averaged LWA and zonal wind in reanalysis products is robust and universal:

$$u_e \approx -\alpha\mathcal{A}, \qquad \alpha > 0. \tag{4}$$

implies that LWA grows at the expense of zonal wind speed and vice versa. The regression coefficient α can be estimated as $\alpha = -(u'_e\mathcal{A}'^T)/(\mathcal{A}'\mathcal{A}'^T)$, where $\mathcal{A}'$, u'_e are row matrices containing the time-filtered transient LWA and zonal wind, respectively. As shown in Fig. 1f, α typically varies between 0 and 1. According to the nonacceleration theorem, $\alpha = 1$ in an idealized barotropic flow. In the presence of baroclinicity and nonconservative processes, the vertical scale of LWA tends to be smaller than that of the zonal wind, which makes $\alpha < 1$ (Huang and Nakamura 2016; Nakamura and Huang 2017). The meridional gradient of α in Fig. 1f reflects the fact that baroclinicity is higher in the extratropics than in the tropics. In the latitudes of storm tracks, α is 0.3-0.4. Equation (4) defines a regional eddy-mean flow interaction that is crucial for block formation in the current context. Note that u_e in Eq. (4) is local departure of the zonal wind from the reference state, and unlike the usual Eulerian definition of eddy, it contains a component that does not depend on the phase of eddy, which we call eddy-induced zonal flow.

c. Traffic jam mechanism and the carrying capacity of the jet stream

With the approximations described in section 2b, NH18 simplified Eq. (2a) into 1D equation:

$$\frac{\partial\mathcal{A}}{\partial t} = \underbrace{-\frac{\partial}{\partial x}\Big((u_0 + c_g^x)\mathcal{A} - \alpha\mathcal{A}^2\Big)}_{\text{Term I}} + S - \mathcal{A}/\tau \tag{5}$$

where the first term of the RHS corresponds to Term (I) in Eq. (2a) with $dx \equiv a\cos\phi d\lambda$, Terms (II)-(IV) (that are of secondary importance) are lumped together as a source and linear damping of LWA, where the cosine factor and angle brackets are dropped for simplicity. Decomposing LWA into steady and transient wave components, $\mathcal{A}(x,t) = \mathcal{A}_0(x) + \mathcal{A}'(x,t)$, transient part of Eq. (5)

may be further written as

$$\frac{\partial \mathcal{A}'}{\partial t} = -\frac{\partial F'}{\partial x} + S' - \frac{\mathcal{A}'}{\tau}, \tag{6a}$$

$$\text{where } F = (C(x) - \alpha \mathcal{A}')\mathcal{A}', \tag{6b}$$

$$\text{and } C(x) \equiv u_0 + c_g^x - 2\alpha \mathcal{A}_0(x). \tag{6c}$$

Away from the source and sink, Eq. (6a) reduces to

$$\frac{\partial \mathcal{A}'}{\partial t} = -\frac{\partial F}{\partial x} = -\left(\frac{\partial F}{\partial \mathcal{A}'}\right)\frac{\partial \mathcal{A}'}{\partial x} \tag{7a}$$

$$= -\left(C(x) - 2\alpha \mathcal{A}'\right)\frac{\partial \mathcal{A}'}{\partial x} \tag{7b}$$

where $\partial F'/\partial \mathcal{A}' = (C(x) - 2\alpha \mathcal{A}')$ is the *effective advective velocity*. Suppose a packet of Rossby wave characterized by $\mathcal{A}'(x,t)$ is propagating eastward (increasing x) in a channel. If $\partial F'/\partial \mathcal{A}'$ is positive everywhere, the packet continues to move eastward across the channel. If on the other hand $\partial F'/\partial \mathcal{A}'$ vanishes somewhere, the front end of the packet stagnates at the location, the flux from behind catches up and LWA accumulates. From Eqs. (7b), (6b) and (6c) and also from Fig. 2 it is evident that $\partial F'/\partial \mathcal{A}'$ vanishes at the the maximum value of F', given by

$$F_c(x) = \frac{C^2(x)}{4\alpha} = \frac{\left(u_0 + c_g^x - 2\alpha \mathcal{A}_0\right)^2}{4\alpha} \tag{8}$$

with the threshold value of LWA at $\mathcal{A}_c'(x) = C(x)/2\alpha = (F_c/\alpha)^{1/2}$.

We call F_c the *carrying capacity* of the jet stream for transient Rossby waves. Carrying capacity arises from the nonlinearity associated with eddy-flow interaction. When the wave amplitude is small, the eastward LWA flux increases with an increasing LWA (Fig. 2). However, as LWA grows, the *effective advective velocity* decreases. This serves as a brake for the advection and eventually the growth of the flux is halted at the carrying capacity when $\mathcal{A}' = \mathcal{A}_c'$. At this point, wave stagnates and the accumulation of LWA starts. Once $\mathcal{A}'$ grows past the threshold $\mathcal{A}_c'$, the LWA flux F' decreases with an increasing LWA (Fig. 2). This reinforces the flux convergence and accelerates the growth of LWA until the flux vanishes. The mechanism of wave stagnation described above is mathematically equivalent to the formation of traffic congestion on a highway, in which an increase

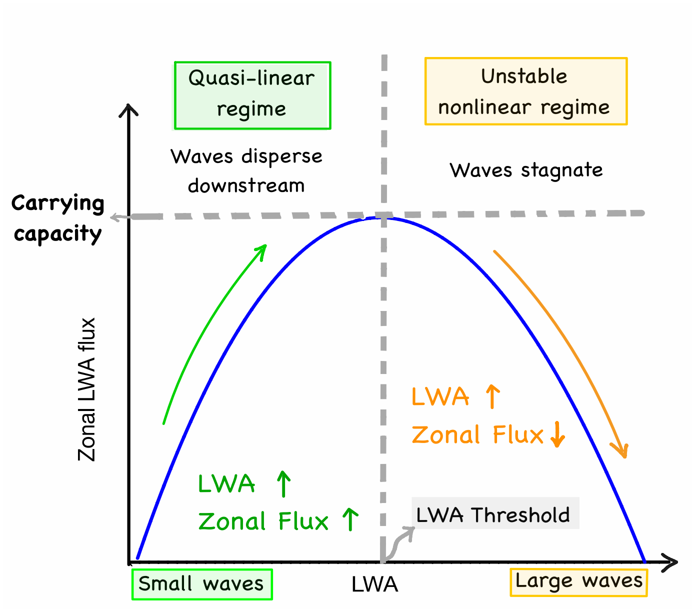

FIG. 2. Schematic showing the relationship between LWA and the zonal LWA flux. For smaller waves (LWA ≪ LWA threshold), the zonal flux of LWA increases with increasing LWA due to the dominant linear term that is associated with an eastward migration of waves with the Doppler-shifted group velocity. For larger waves, (LWA ≥ LWA threshold), the flux decreases with increasing LWA due to the dominant nonlinear term associated with the eddy-induced zonal flow. The 'carrying capacity' is the maximum zonal LWA flux that can be transmitted at any location. To reach the nonlinear regime the incident zonal LWA flux must be elevated to this level. If the incident flux from upstream is sustained, the nonlinear regime creates a positive feedback between the flux convergence and increase in LWA and therefore it is unstable, spontaneously evolving toward the zero-flux (blocked) state. A low carrying capacity in the jet stream is conducive to block formation since it requires less flux perturbation from upstream to reach the nonlinear regime. Also see Figs. 5d and 6b.

in the traffic density causes a decrease in the traffic speed [analogus to Eq. (4)] (Lighthill and Whitham 1955, Richards 1956). In places where the carrying capacity F_c is low [i.e. due to an enhanced stationary wave $\mathcal{A}_0(x)$ or a reduced mean jet-speed (u_0)], the threshold $\mathcal{A}_c$ is also low and thus it is easier for a block to form for the same level of incident wave-activity flux F'.

With simple 1D and 2D models, Nakamura and Huang (2017) demonstrate that edge waves traveling along a PV front can stagnate and form an abrupt transition from zonal propagation into a block-like stationary structure through this mechanism. The boundary of the transition then migrates slowly upstream.

While the traffic jam analogy provides a simple theory for block formation, given the diversity of block manifestations, it is worth testing the extent to which the theory characterizes blocking events observed in the real atmosphere. In what follows, we analyze a large number of wave events that involve persistent, anomalous meandering of the jet stream during the Northern Hemisphere winter with the ERA5 reanalysis product. We then explore the extent to which the imprint of traffic jam is recognizable in the blocking statistics. In particular, we examine how the theoretical *carrying capacity* of the jet stream relates to the frequency and duration of the observed blocks and how the wave-activity budget evolves during the lifecycle of blocking.

3. Treatment of data and methods

a. Evaluation of the budget terms

We use 6-hourly horizontal velocities and temperature from ERA5 on 37 pressure levels with a $1^\circ \times 1^\circ$ horizontal resolution (Hersbach et al. 2020) to compute the terms in the LWA budget for the Northern Hemisphere winter (DJF 1979-2022). In addition to the vertically-averaged LWA, all terms in the second column of Table 1 are computed following the same procedures as in Neal et al. (2022); Huang and Nakamura (2016, 2017); Nakamura and Huang (2018). Once evaluated, these quantities are daily averaged for further analysis. The transient component of the LWA and the transient fluxes (e.g. $\mathcal{A}'$, F'_λ, F'_ϕ etc.) are calculated by applying a 4-day low-pass time filter on daily-averaged time series. Prior to the temporal filtering we also remove the seasonal cycle from the time series which is computed using the first three annual harmonics of the daily means of the entire dataset which spans from Dec. 1979 to Feb. 2022. After the temporal filtering, we zonally smooth the transient fields using a 15° running-mean along longitude. The latter is done to suppress variability associated with the phase structure of the small-scale traveling waves. While the smoothing does not change the overall results, it improves the description of the wave activity budget associated with large-scale waves as discussed in the subsequent sections.

b. Empirical estimates of various parameters

A key quantity in this study is the seasonal-mean 'carrying capacity' for the transient eddy, F_c [Eq. (8)]. To evaluate F_c, we need to evaluate α, $\mathcal{A}_0$ and $u_0 + c_g^x$ [see Eq. (8)]. α represents the wave-mean flow interaction strength and is determined from Eq. (4) (see Fig. 1f). $\mathcal{A}_0$ represents

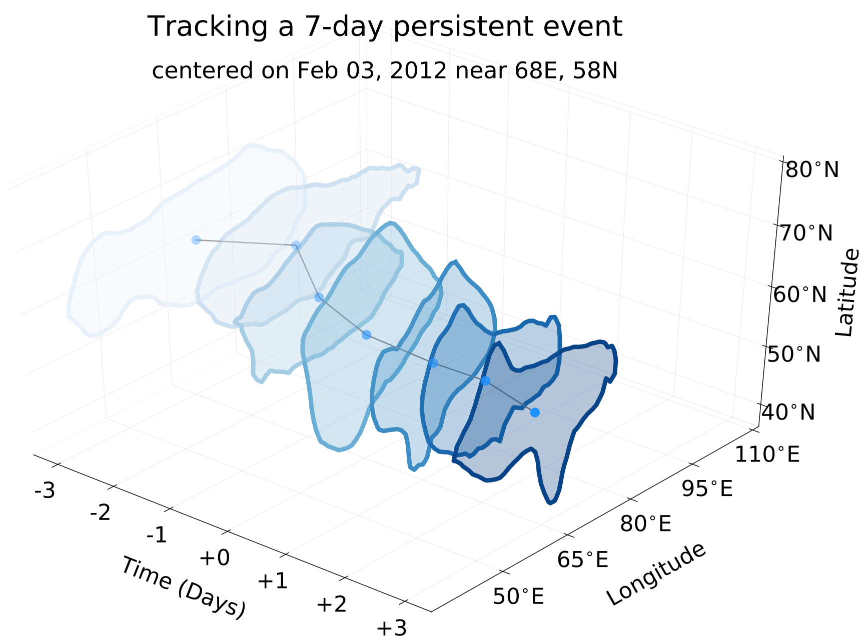

FIG. 3. An example of a blocking event on February, 03, 2012 (day 0) at 68°E, 58°N extracted from daily-averaged LWA field using the feature-tracking algorithm as outlined in Section 3. The blue connected patches are regions where $\mathcal{A}\cos\phi \geq \mathcal{A}_c\cos\phi$. Two consecutive patches have more than 60% areal overlap and the light to dark shading indicates progression of time.

a stationary (and steady) wave component maintained by external forcing such as topography and land-sea thermal contrast. In this study, $\mathcal{A}_0$ is computed for each longitude and latitude using the monthly-mean QGPV in Eq. (1) and averaged over the season (Huang and Nakamura 2017; Nakamura 2024). $\mathcal{A}_0$ calculated this way is distinct from the time-mean LWA and minimizes the effect of blocks on the stationary LWA. $\mathcal{A}_0$ computed as the local seasonal minimum in LWA (as in NH18) gives qualitatively similar result (not shown). Finally, $u_0 + c_g^x$ represents the Doppler-shifted zonal group velocity of Rossby wave-packet and is computed as a regression coefficient between vertically-averaged linear zonal LWA flux $(F_1 + F_3)$ and the wave-activity $(\mathcal{A}\cos\phi)$ [see Table 1].

To highlight the role of stationary wave in the variation of F_c, we use the zonally averaged values of $u_0 + c_g^x$ and α (denoted by an overbar). Since the zonal variation in these quantities is modest, this averaging does not affect the overall structure of F_c, while it filters spurious values in isolated regions where the estimate of α is unreliable. The structure of F_c and its decomposition will be discussed later (Figs. 6b and C1 of appendix C.)

c. Identification and tracking of wave-activity blocks

Blocking events are identified as dynamical features where: (1) daily-averaged LWA contours exceed the threshold of $\mathcal{A}_c \cos\phi = 65$ ms^{-1} and where (2) the LWA contours persist over a location for 4 days or more. The threshold value, $\mathcal{A}_c \cos\phi$ is empirically determined by finding an aggregate estimate of $\mathcal{A}\cos\phi$ that maximizes F_λ between 30-60°N during DJF. See appendix B for more details. The 'blocked' wave-activity events are then traced using a feature-tracking algorithm as described below. Note that no additional temporal or spatial filtering is applied to LWA inside the tracking algorithm.

1. From the daily-mean LWA maps on the longitude-latitude plane, the large wave-activity events are identified as isolated patches in which $\mathcal{A}\cos\phi \geq 65$ m s^{-1}.

2. Two consecutive patches 24 hours apart are considered to be part of the same event if the area of overlap is at least 60% of their average area, otherwise they are deemed as separate events.

3. Step 2 is iterated in a sliding time window of 25 days for each winter season (DJF) until no significant overlap is found. Specifically, the search for overlapping patches ends and a 'blocked' wave-activity event is identified when their areal overlap reduces below 60%.

4. For every event, its location is determined by finding the centroid of the overlapping patches and its persistence is determined by counting the number of consecutive days during which the patches overlapped around the centroid. All events that persist for less than 4 days are discarded from the analysis.

5. Every event is further classified as either cyclonic or anticyclonic depending on the dominant sign of the QGPV anomalies. The event is deemed cyclonic (anticyclonic) if the QGPV anomaly (q_e) at the centroid averaged over the duration of the event is positive (negative). [See Valva and Nakamura (2021); Chen et al. (2015).]

6. Steps 1-5 are repeated for 43 winters from 1979-1980 to 2021-2022.

Figure 3 illustrates the identification of a blocking event using the steps described above. Figure 4 shows a composite lifecycle of 72 blocks that persisted 7 days or longer according to the method described above. All events identified by this process closely resemble the canonical structure of an atmospheric block, including anomalous growth of wave amplitude (Figs. 4a) accompanied

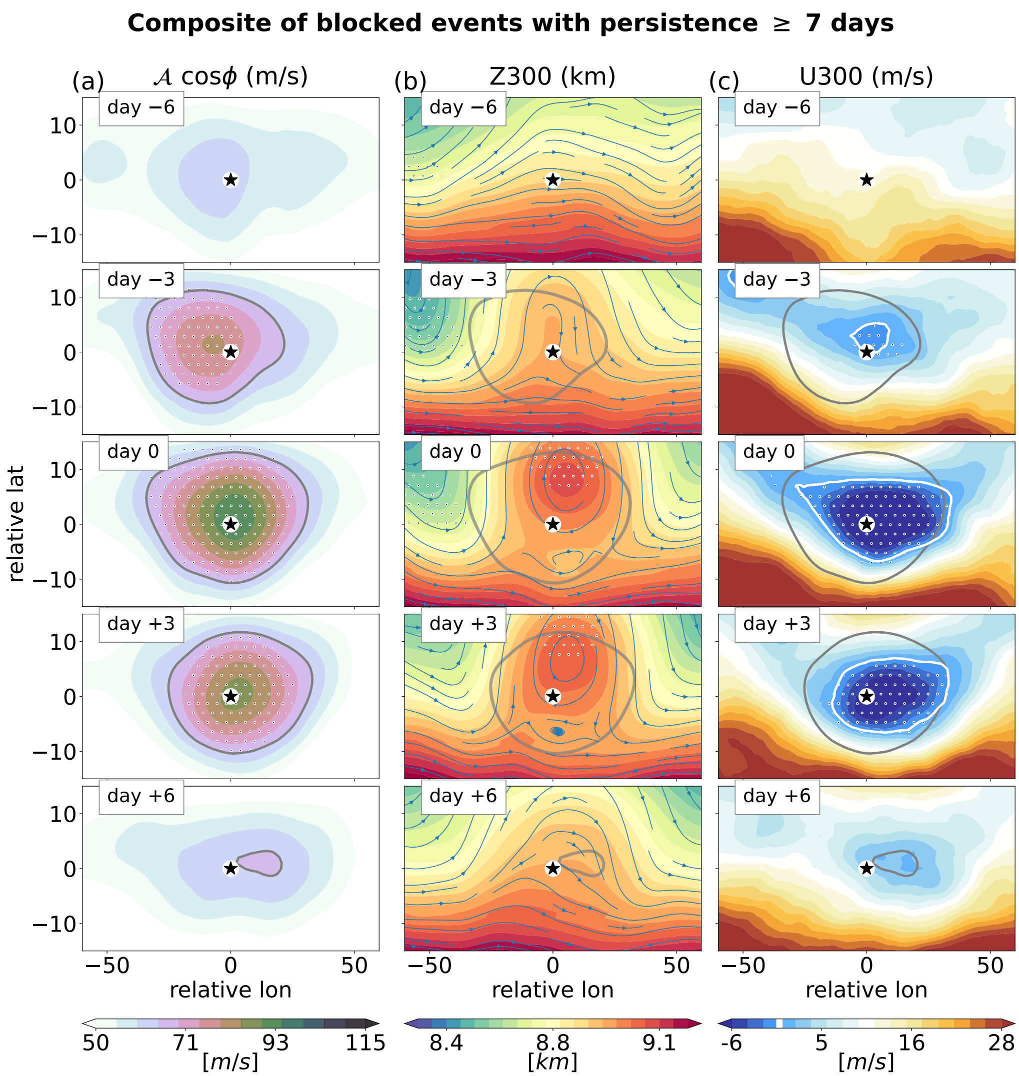

Fig. 4. Composite lifecycle of wave-activity blocks with persistence ≥ 7 days showing time evolution of (a) vertically averaged LWA in ms^{-1}, (b) geopotential height at 300 hPa in km (colors), wind streams at 300 hPa (blue streamlines) and (c) zonal wind speed at 300 hPa in ms^{-1}. The composite is obtained from a sample of 72 events. The regions with white dots indicate statistically significant values outside a confidence interval (CI) of $15-85$ percentile estimated from 5000 bootstrap samples. The gray contours encircle the region where $\mathcal{A}\cos\phi \geq \mathcal{A}_c = 65$ m s^{-1} and the white contours in column (c) encircle regions where $u_{300} < 0$. The x,y axes are longitude and latitude centered on the blocking location on day 0 indicated by the black star at the origin.

by a persistent geopotential anomaly and a poleward diversion of the jet stream (Fig. 4b), and local deceleration of zonal winds at 300 hPa (Fig. 4c). Therefore, we refer to these persistent anomalous LWA events as *wave-activity blocks*. Due to predominance of anticyclonic blocks at this persistence (≥ 7 days), the composite lifecycle also appears to be anticyclonic. In Fig. D1 we show a similar composite for 399 events with shorter persistence (4-6 days). At this persistence the samples also include a large fraction of cyclonic events, and at the peak (day 0 to 2) the 300 hPa geopotential height exhibits an anticyclonic-cyclonic pair reminiscent of a Rex block. A more detailed comparison of various blocking types and their persistence is deferred to a future study.

4. Results

a. Spatial distribution and persistence of blocking events

The spatial distribution of the wave-activity blocks during NH winter is shown in Fig. 5. The majority of the short-lived (≤ 3 days) events occurs more or less homogeneously throughout the midlatitudes (not shown). However, long-lived events with persistence ≥ 4 days tend to occur in clusters over the pre-existing quasi-stationary ridges and troughs over the North Atlantic and Pacific storm tracks (Figs. 5a, c). The clusters of wave-activity blocks are found in the close vicinity of the peaks in the stationary LWA ($\mathcal{A}_0 \cos\phi$, Fig. 5b). A particularly strong stationary LWA to the north of the North Atlantic cluster is associated with a pronounced poleward excursion of the low-level time-mean QGPV due mainly to the sea surface temperature distribution.

The identified events are further classified into cyclonic or anticyclonic types using the method described earlier. The exact location, frequency and persistence of the two block types are found to vary by longitude as revealed by their zonal distribution (see Fig. 5c). The cyclonic blocks (red bars in Fig. 5c) are found to be fewer in number; they show a peak activity over the east coast of Eurasia (120°E - 150°E), coincident with climatological low-pressure system at 300 hPa (Figs. 5a, c). In contrast, the anticyclonic blocks (blue bars in Fig. 5c) dominate the rest of the NH with a particularly large frequency around the west coast of Europe (30°E - 30°W), coincident with climatological high-pressure system at 300 hPa (Figs. 5a, c) and the peak stationary LWA (Figs. 5b, c). Overall, the frequency of wave-activity blocks correlates with the strength of the stationary LWA averaged between 40−60°N (maroon curve in Fig. 5c).

Qualitatively, the overall distribution of wave-activity blocks reproduces the previously identified regions of high blocking activity based on other metrics (Barriopedro et al. 2006; Pelly and Hoskins 2003). The overlap of the climatological mean stationary LWA and the wave-activity blocks agrees well with the prediction of NH18 and Paradise et al. (2019), who state that the modulation of the

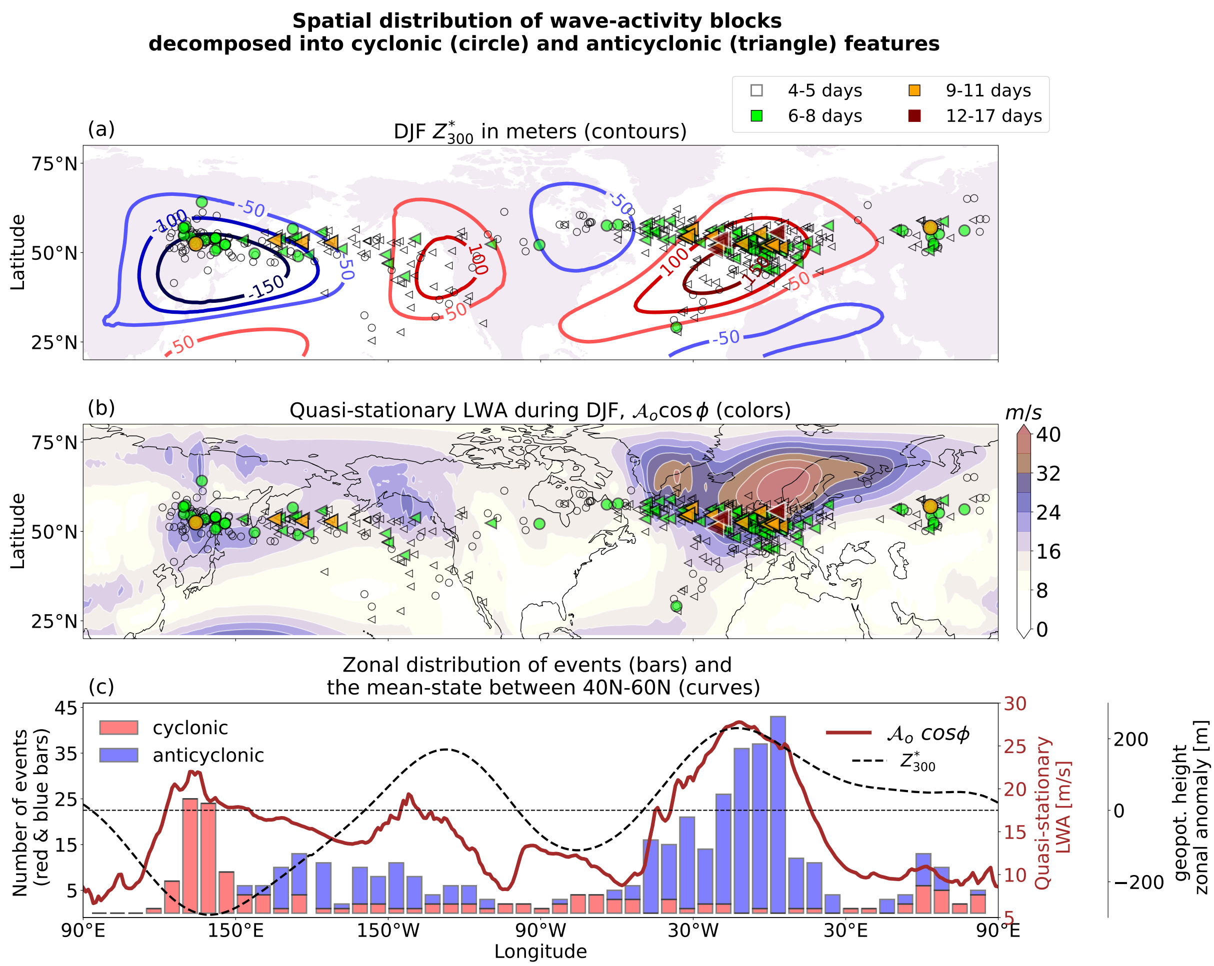

FIG. 5. Spatial distribution of wintertime wave-activity blocks identified by the feature-tracking algorithm described in section 3c. (a) Locations at day 0 for cyclonic (circles) and anticyclonic (triangles) events, color-coded according to persistence (4-17 days). Contours are the climatological mean DJF 300-hPa geopotential height anomaly (departure from the zonal mean). (b) Same as (a) but overlaid with the DJF-mean stationary LWA $\mathcal{A}_0 \cos\phi$ (color shading). (c) Histogram of events decomposed into cyclonic (red) and anticyclonic (blue) features in the NH. The curves represent the DJF-mean geopotential height anomaly at 300hPa (black dashed curve) and DJF-mean stationary LWA ($\mathcal{A}_0 \cos\phi$) averaged between 40°-60°N. All data is from ERA5 reanalysis during DJF from 1979 to 2022.

jet speed by a steady, forced Rossby wave provides bottlenecks to the transient eddies and localizes block formation. In agreement with this idea, recent modeling work by Narinesingh et al. (2020) also showed the importance of topographically forced stationary Rossby waves on the persistence of blocking.

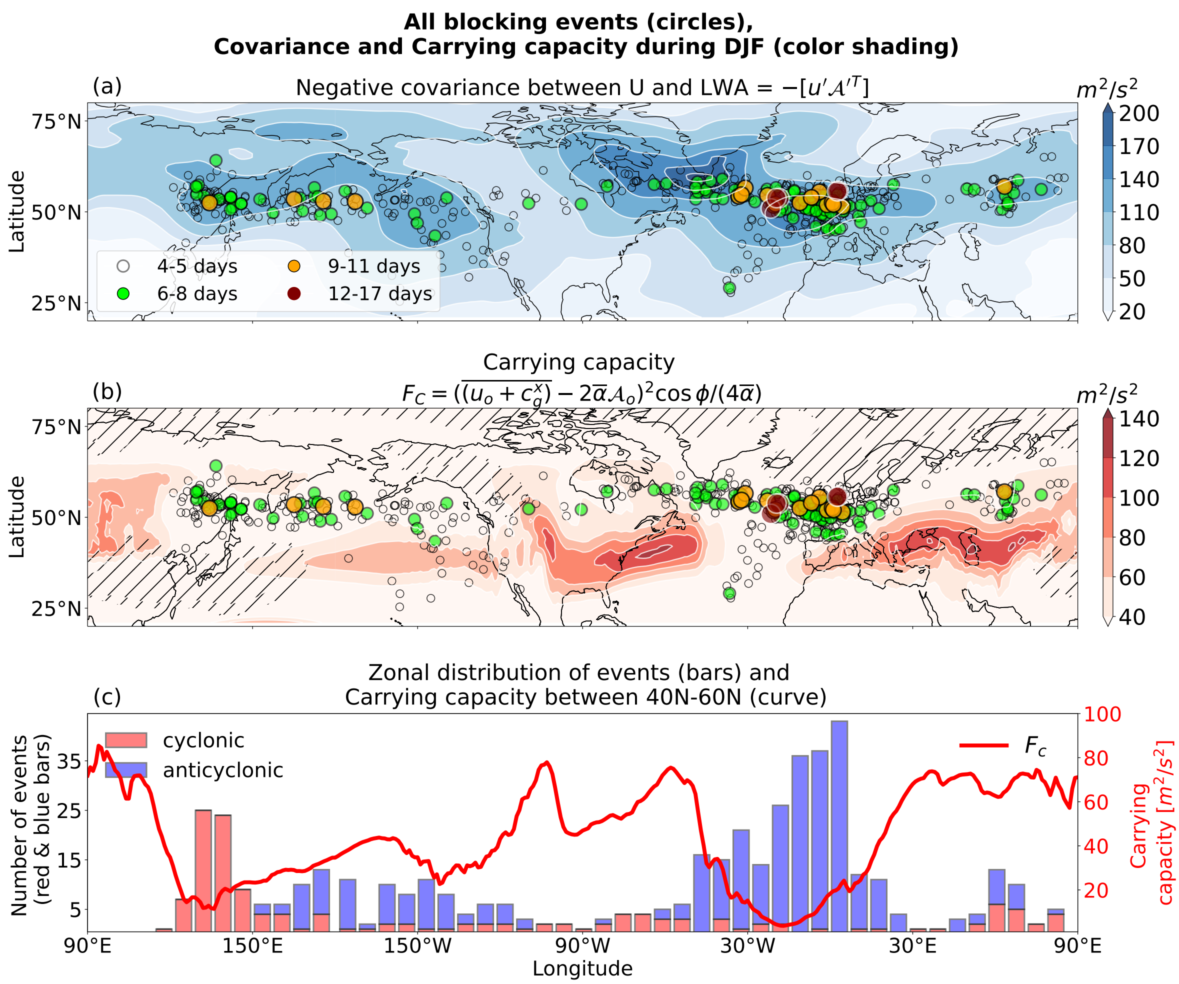

FIG. 6. (a) Covariance relation between transient zonal-wind and wave-activity. Blue is negative and is shown in absolute values. (b) Theoretical carrying capacity for transient LWA during NH winter (color-shading) estimated using Eq. (8). Both (a) and (b) are overlaid with the spatial distribution of wave-activity blocks as in Fig. 5a (circles). The black stripes in (b) denote regions where the transient zonal-wind and wave-activity are weakly correlated, i.e. where r-value < |0.5| in the estimation of α. (c) Same as Fig. 5c but overlaid with the carrying capacity for the transient eddies (F_c). All data is from ERA5 reanalysis during DJF from 1979 to 2022.

b. Eddy-wind covariance and carrying capacity

Next, we evaluate whether the wave-activity blocks satisfy some of the theoretical constraints for the traffic jam mechanism described in section 2c. Figure 6a clearly shows that wave-activity events persist in locations where the negative covariance between transient zonal wind and LWA is pronounced, consistent with Eq. (4). This shows that the regional eddy-flow interaction is symptomatic for block formation.

More importantly, Figs. 6b and c demonstrate that wave-activity blocks tend to persist longer in locations where the carrying capacity for transient eddies (F_c), is lower, whereas they are sparse and short-lived in locations where F_c is higher. Figure 6b shows that large F_c coincides with fast subtropical jet streams, and persistent blocks are situated almost invariably to the north of these regions, where F_c is smaller. Some short-lived events occur in the subtropics of the eastern North Pacific and eastern North Atlantic. These events are mostly related to equatorward breaking of synoptic eddies spun off from the storm tracks. The longitudinal profile of F_c in Fig. 6c shows that it almost vanishes in the eastern North Atlantic (~20°W) and also remains small over the Pacific (130°E-140°W). There is a clear correlation between the minima in F_c and the frequency of the blocks. In particular, the very small F_c over the Atlantic leaves little room for transient eddies to pass though this region without reaching the nonlinear regime (Fig. 2), which explains well the very high peak frequency of blocks in the Euro-Atlantic sector in light of the traffic jam theory.

Note that the carrying capacity encapsulates two competing physical processes [see Eqs. (6c) and (8)], namely, eastward flux of transient LWA by the Doppler-shifted group velocity $(u_0 + c_g^x)$ and a reduction in the eastward advective flux due to stationary wave-flow interaction $(-2\alpha\mathcal{A}_0)$. A stronger, more zonally symmetric jet would raise the capacity and inhibit the block formation, while a stronger wave-flow interaction would lower the capacity and favor block formation. This feature is captured by F_c through the numerator, $(u_0 + c_g^x - 2\alpha\mathcal{A}_0)^2$. See Fig. C1 for a decomposition of F_c into separate contributions.

So far we have discussed how the climatological mean state of the midlatitudes affects the location and persistence of the extreme LWA events. While the result is broadly consistent with the traffic jam theory, a more direct test would be how LWA and its budget evolve during the lifecycle of the blocking events, which we will explore next.

c. 1D composite lifecycle of wave-activity blocks

Figure 7a shows composite lifecycle of wave-activity blocks with a persistence of 7 days or longer in terms of their vertically averaged transient LWA budget [Eq. (2a)]. Before forming the composite, each of the budget terms is first temporally filtered by removing the seasonal cycle and

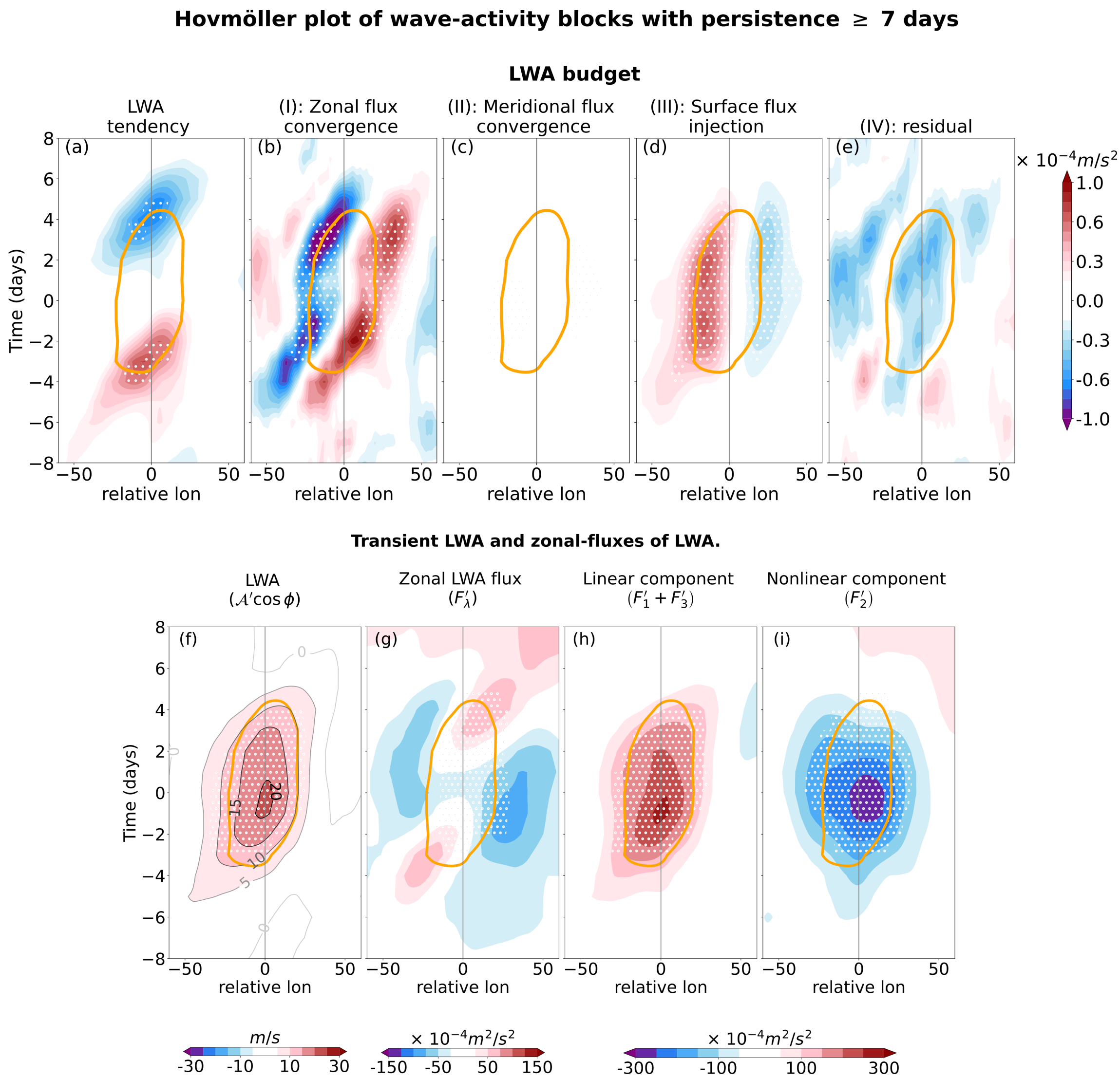

Fig. 7. 1D composite lifecycle of wave-activity blocks with persistence ≥ 7 days in terms of their vertically-averaged transient LWA budget in the top row (panels a-e) along with the evolution of transient LWA and zonal-LWA fluxes in the bottom row (panels f-i). Each panel shows (a) LWA tendency, (b) zonal flux convergence, (c) meridional flux convergence, (d) surface flux injection, (e) the residual, (f) transient LWA, (g) the transient zonal flux of LWA and the latter's decomposition into (h) linear and (i) nonlinear components. The composite is obtained from a sample of 72 events. All fields are meridionally averaged between ±15 degrees of the centroid latitude. The stippled regions indicate statistically significant values outside a confidence interval of $15-85$ percentile. The error range is estimated from 5000 bootstrap samples picked from a set of random locations in the NH and random 15-day time slices during DJF from 1979-2022. The yellow contours encircle the region where $\mathcal{A}\cos\phi \geq \mathcal{A}_c\cos\phi$.

applying a 4-day low-pass time filter followed by a zonal smoothing using 15° running mean. The filtered terms are then averaged meridionally over ±15 degrees of the centroid latitude at the peak of each event identified via the tracking algorithm. Finally, the terms are composited and plotted as functions of longitude and time, both centered on the peak of the events.

The growth and decay phases of the block are well separated by a period of near-steady amplitude (mature phase) for ~6 days (Figs. 7a, f). During the growth and decay phases, the change in LWA proceeds from upstream (west) to downstream (east) (Fig. 7a). These LWA tendencies are balanced by the combination of the zonal flux convergence (Fig. 7b), surface injection (Fig. 7d), and the residual (Fig. 7e). Due to the meridional averaging, the effect of meridional flux convergence is weak (Fig. 7c). The positive (negative) LWA tendency largely reflects the zonal flux convergence (divergence) (Figs. 7a, b). During the growth phase, a positive LWA flux is fed from upstream, whereas during the decay phase, a positive flux is discharged downstream (Fig. 7g). The upstream flux starts ∼ 40 degrees to the west of the block's center around day -5, whereas the downstream flux extends to ∼ 30 degrees east of the block and lasts to about day +5, with a sign of continuation further downstream. During the mature phase, while LWA achieves a peak value, the zonal flux vanishes and even turns slightly negative inside the block (Figs. 7f, g). Further decomposition of the zonal flux into linear and nonlinear fluxes [Eq. (2b)] reveals that, while the linear flux is positive and maximal in the block, the nonlinear flux grows strongly negative and suppresses the linear flux at the peak of the block (Fig. 7h, i). This is consistent with the traffic jam theory. Notice that the zonal flux has peak negative values outside the block during the mature phase (Fig. 7g), which creates weak divergence (convergence) in the upstream (downstream) of the block (Fig. 7b). The divergence of the flux in the upstream region is largely balanced by a positive surface injection due to a poleward flux of eddy potential temperature at the surface, whereas the convergence in the downstream region is largely balanced by a negative surface injection due to an equatorward flux of eddy potential temperature (Figs. 7b, d). As a result, the budget of vertically-averaged LWA in the mature phase does not create a significant net tendency of LWA. The residual term is predominantly negative inside the block, suggesting that LWA is dissipated through mixing of QGPV. However, there is a pocket of positive values in the upstream of the block between day -5 and -3, suggesting that diabatic heating may have some role in generating the upstream flux (Neal et al. 2022; Steinfeld et al. 2020) (Fig. 7e).

There is a fair amount of agreement between Fig. 7 and the traffic jam theory. Specifically, the block formation is triggered by an incident LWA flux from upstream, followed by the suppression of the zonal flux by the eddy-induced wind. Yet there are some important deviations from the theory. For example, the composite lifecycle is symmetrical in longitude about the center of the block. In the 1D traffic jam model, the growth phase involves shock formation and LWA amplification on the upstream side of the block (Nakamura and Huang 2017, 2018), which is characteristically absent in Fig.7. This is presumably due to a limitation of the 1D model. Nakamura and Huang (2017) shows that in a 2D model a near-discontinuity in LWA still forms but its location is not independent of latitude and therefore it is likely smoothed by the meridional averaging. More intriguing is the timing of the decay phase. The traffic jam theory explains the onset mechanism for a block, yet it does not provide insight for its demise other than a prescribed damping time scale (representing the mixing of QGPV). It remains to be seen whether the theory may be used to predict the decay and persistence of the block.

Figure D2 shows a similar analysis for the 399 events with shorter persistence (4-6 days). The overall budget evolution is similar to the more persistent events in Fig. 7, but the separation of the growth and decay phases is much shorter, and the zonal flux convergence and divergence form straight diagonal stripes (Figs. D2a,b). Although the growth phase is characterized by a positive influx of wave-activity from upstream, the decay phase is characterized by a negative (westward) dispersal of wave-activity mainly due to the nonlinear flux (Figs. D2g,i).

d. 2D-composite lifecycle of wave-activity blocks

Since atmospheric blocks involve meridional diversion of the jet stream and transient eddy, the 1D analysis at the centroid latitude does not capture the full details of block's lifecycle. Here we focus on the 2-dimensional view of the LWA budget evolution during the growth and decay phases of the wave-activity blocks.

Figure 8 shows the 2D composite lifecycle of those wave-activity blocks which persist for at least 7 days. The growth (decay) of wave amplitude is captured by the positive (negative) sign of the LWA tendency (column a). Even though the LWA tendency is localized to the vicinity of the block's center, the three flux convergence terms along with the residual (columns b-e) have either a quadrupolar or a dipolar structure at the periphery of the block with the strongest magnitudes on

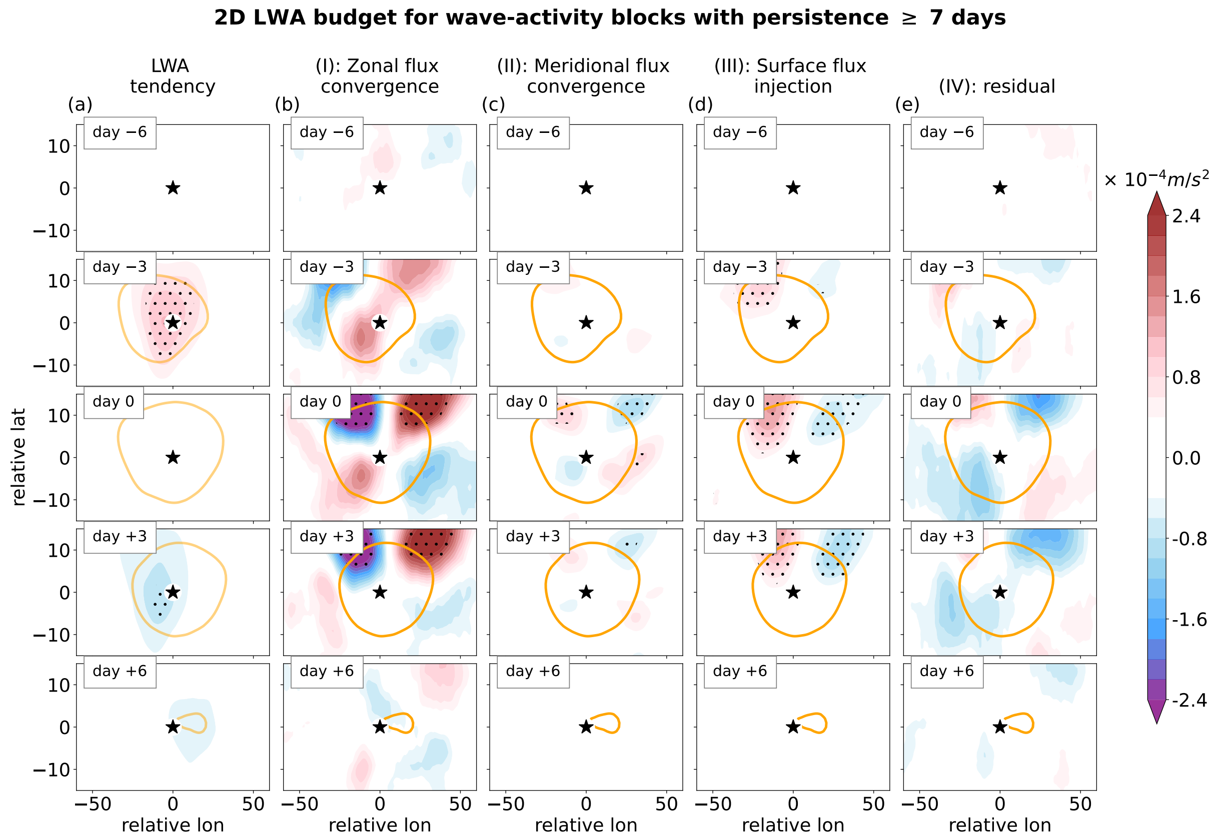

FIG. 8. 2D composite lifecycle of wave-activity blocks with persistence ≥ 7 days shown by the vertically averaged transient LWA budget. Each of the budget terms in Eq. (2a) is shown in columns (a) through (e) and each row shows their time evolution from day −6 to day +6 at an interval of 3 days. Sum of (b)-(e) equals (a). The composite is obtained from a sample of 72 events and centered on the location of the peak LWA on day 0. The regions with black dots indicate statistically significant values outside a confidence interval of 15 − 85 percentile estimated from 5000 bootstrap samples. The yellow contours encircle the region where $\mathcal{A}\cos\phi \geq \mathcal{A}_c\cos\phi$.

the poleward side. This is related to the fact that both the jet and eddies are deflected northward around the block. [Also note that the peak geopotential height anomaly is situated to the north of the wave-activity block (Fig. 4b).]

Consistent with Fig. 7a, during the growth phase (day -3), the positive tendency near the center of the block is largely attributable to the zonal flux convergence (Figs. 8a,b). However the zonal flux convergence extends to the northeast of the block, where it is balanced by the surface injection and the residual (Figs. 8b,d,e). There are also bands of zonal flux divergence to the northwest and southeast sides of the block, which are evenly balanced by the other budget terms (Figs. 8b-e.)

During the mature phase (day 0), the budget terms are all small at the center of the block but a strong quadrupolar structure appears in the zonal flux convergence (Fig. 8b), which is balanced by the other three budget terms to a varying degree. Both the meridional flux convergence and the surface injection, though small at the center, are significant to the north (Fig. 8c,d), whereas the residual is weakly positive to the northwest and southeast of the block's center and strongly negative to the northeast and southwest (Fig. 8e). The overall structure of the budget terms remains similar into the decay stage (day +3), but the diminished zonal flux convergence makes the LWA tendency negative on the east side of the block (Fig. 8a,b.)

Figure 8 paints a significantly more complex picture than the 1D traffic jam model due to the meridional deflection of eddies by a meandering jet around the block (see Polster and Wirth 2023 for a related discussion). Through the maturation phase, the surface injection is positive (negative) to the northwest (northeast) of the block where the near surface meridional flux of potential temperature is positive (negative) (Fig. 8d). There is also a hint of nonconservative sources of LWA to northwest and southeast of the block (Fig. 8e), presumably due to diabatic effects (Neal et al. 2022), although overall negative values of the residual (damping due to mixing of QGPV) dominate. These local sources and sinks of column-mean LWA is balanced by the horizontal convergence/divergence of the LWA flux around the block.

A more detailed view of the horizontal flux of LWA and the zonal flux convergence is shown in Fig. 9. The vectors represent the flux (F'_λ, F'_ϕ) in column (a), its linear part $(F'_1 + F'_3, F'_\phi)$ in column (b) and the nonlinear eddy-induced part $(F'_2, 0)$ in column (c). Here the prime denotes transient eddies, i.e. 4-day low-pass time filtered fields with the seasonal-mean removed. These vectors may be thought of as the effective group velocity $(\vec{c_g})$ of the Rossby waves multiplied by LWA, where the linear flux vectors indicate eastward transmission of a Rossby wave packet by the Doppler-shifted zonal group velocity $(u_0 + c_g^x, c_g^y)$ and the nonlinear flux vectors indicate its relative westward Doppler shift due to eddy-induced winds. The color indicates the corresponding zonal flux convergence (the meridional flux convergence is relatively small and not included).

From the onset phase (row 1 in Fig. 9) to the mature phase (row 2), both the eastward linear fluxes and the westward nonlinear flux grow, but they occupy different areas of the block. The linear fluxes dominate in the region slightly north of the centroid, whereas the nonlinear flux dominates in the region slightly south of the centroid. As a result, the sum of the two fluxes produces a

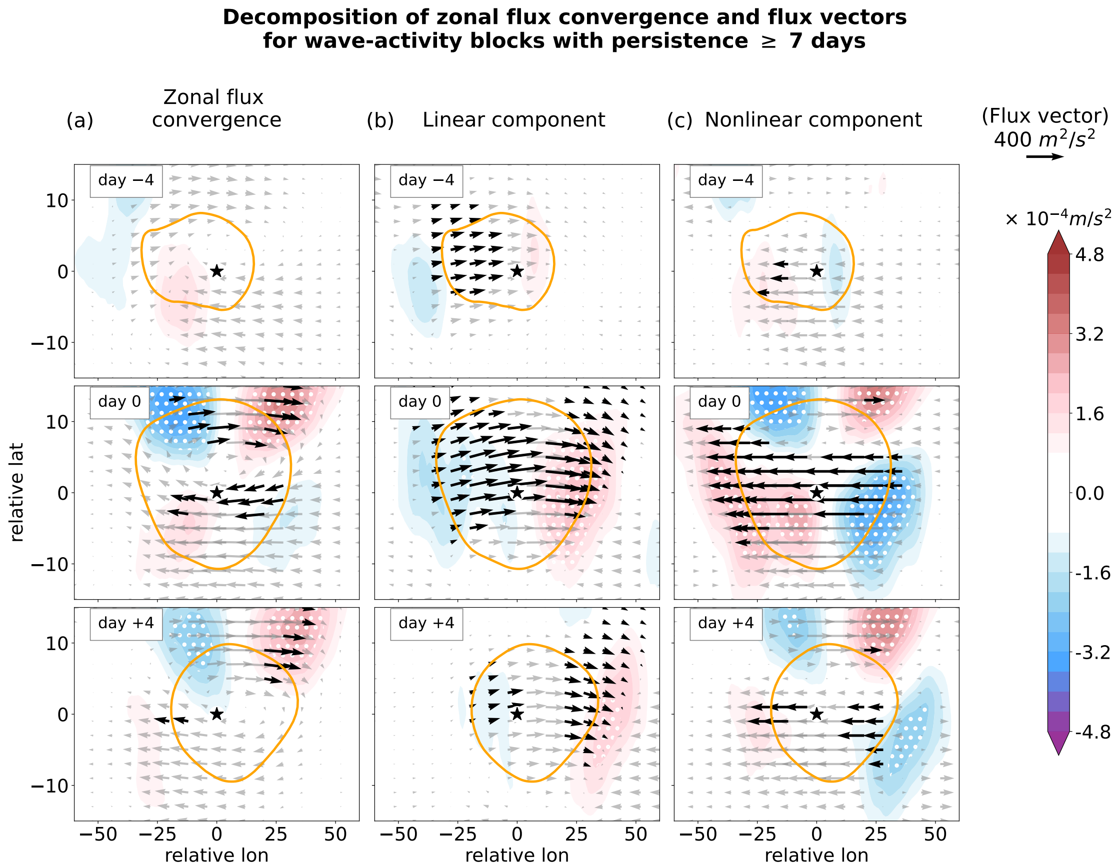

FIG. 9. Same as Fig. 8 but for the 2D composite lifecycle of (a) zonal LWA flux convergence (colors) and horizontal wave-activity flux vectors (F'_λ, F'_ϕ) and its decomposition into (b) linear and (c) nonlinear components for wave-activity blocks with persistence ≥ 7 days.The composite is obtained from a sample of 72 events, where each column shows their evolution from day −4 to day +4. The regions with white dots indicate statistically significant flux convergence values outside a confidence interval of 15 − 85 percentile and the black vectors indicate statistically significant flux values outside a confidence interval of 25 − 75 percentile estimated from 5000 bootstrap samples. The yellow contours encircle the region where $\mathcal{A}\cos\phi \geq \mathcal{A}_c\cos\phi$.

clockwise circulation of LWA around the center of block (Fig. 9a), effectively suppressing the net eastward movement of the entire block. During the decay phase (row 3 in Fig. 9), both linear and nonlinear fluxes weaken, but the linear fluxes surpass the nonlinear flux in the northeast corner of the block, whereas the nonlinear flux surpasses the linear flux in the southwest corner. Either way LWA is drawn out of the block, and this leads to its decay.

In summary, the 2D analysis reveals a circulation of LWA inside the block, which is inaccessible with the meridionally averaged 1D analysis. In particular, the meridionally staggered placement of the eastward linear fluxes and the westward nonlinear flux leads to a rotational flux of LWA around the block, consistent with the sign of the QGPV anomaly.

5. Concluding remarks

It is well known that there is vast diversity in morphology, geographical locations, size and persistence of atmospheric blocking (Woollings et al. 2018, Lupo 2021). The present study aims at extracting common dynamical processes that define blocking lifecycle through the lens of local wave-activity budget. We have developed a feature tracking algorithm to detect persistent ($\geq$ 4 days) anomalous Rossby wave events in the NH winter and analyzed their composites of wave-activity budget. The main findings are summarized as follows:

1. All persistent events identified by large values of LWA (wave-activity blocks) exhibit typical properties of an atmospheric block such as anomalies in geopotential height, poleward diversion of the jet stream and local wind reversal (Fig. 4).

2. The wave-activity blocks are found in two predominant clusters - the North Atlantic and North Pacific clusters. The majority of the blocks is anticyclonic, although a small cluster of cyclonic blocks is found over the east coast of Eurasia. The frequency of blocks is highest in the Euro-Atlantic sector (Fig. 5).

3. Blocks are preferentially formed in the vicinity of large stationary LWA (Figs. 5b, c). These are also the regions where wave activity and zonal wind covary negatively, underscoring the importance of eddy-flow interaction for the block formation (Fig. 6a).

4. Blocks are found to be collocated with regions of lower ‘carrying capacity’ for transient eddies, broadly consistent with the traffic jam mechanism of NH18 (Figs. 6b, c).

5. The composite lifecycle of long-lived blocks reveals that the zonal flux convergence of LWA dominates the LWA tendency during the growth and decay phases. The meridional eddy momentum flux divergence plays little net effect. During the mature phase, the positive (negative) surface injection of LWA in the upstream (downstream) region is balanced by the zonal flux convergence of the opposite sign in the respective region. While the residual of the

budget is broadly negative inside the block, suggesting a loss of LWA through mixing, there is also a hint of diabatic LWA source in the upstream of the block during the onset (Figs. 7a-e). Although the tendency of LWA has greatest signal around the center of the block, the budget terms have large (and compensating) values at the periphery during the lifecycle due to the meridional diversion of the jet stream and eddies around the block (Fig. 8).

6. In the composite lifecycle, the zonal flux is controlled by two competing processes, (i) downstream transmission of Rossby waves Doppler-shifted by the background jet and (ii) upstream advection by eddy-induced wind. At the peak of the block, the waves are primarily stalled by the latter (Figs. 7a,h,i). However, the compensation of the two does not necessarily occur at the same locations, leading to a rotational flux of LWA within the block (Fig. 9).

Despite substantial variation among individual events, the composite analysis suggests that on average the wave-activity blocks may be understood by the traffic jam mechanism. The conceptual 1D traffic jam model explains why large-amplitude waves get blocked while small-amplitude waves do not and why there are some preferential locations for block formation (NH18).

While the emergent conceptual picture is fairly simple, there are some limitations within the theory that is worth recognizing. First, the LWA framework does not inform about the source of zonal influx. In fact, various factors could trigger an increase in the flux upstream which may eventually lead to a spontaneous block formation. This includes diabatic heating (Tilly et al. 2008; Steinfeld et al. 2020; Neal et al. 2022), stratospheric forcing (Woollings et al. 2010a; Li et al. 2024) and disturbances from the tropics (Henderson et al. 2016; Gollan and Greatbatch 2017). Second, the theory is based on the budget of vertically-averaged LWA and assumes that the dynamics is barotropic. Although the low-frequency circulation of the NH winter contains a large barotropic component (Blackmon et al. 1977 section 8a), there is significant 3D structure associated with blocks and their precursors (Nabizadeh et al. 2021, Martineau et al. 2022). We suspect that this is one of the reasons why there is large scatter in the column-mean flux of LWA about its mean (Fig. B1a). For the same reason, any given blocking event may show deviations from the idealized barotropic traffic jam mechanism.

Nevertheless, to the extent that the statistics of blocks are concerned, it is hoped that the theory can be used to make a probabilistic estimate of the long-term changes in the blocking statistics by predicting the changes in the carrying capacity over intraseasonal timescales (Liu and Wang

2024) or under climate change scenarios as has been demonstrated by Paradise et al. (2019) in a toy model. The theory can also be used to improve our understanding of the dynamical link between blocking biases and mean-state biases in climate models (Scaife et al. 2010; Vial and Osborn 2012; Davini and D'Andrea 2016; Polster and Wirth 2023). Meanwhile, we still do not have a viable theory for the duration/persistence of blocking. Future work will address these issues using global climate simulations and idealized GCM experiments.

Acknowledgments. A majority of this work was done during the final year of PB's PhD research. We thank Tiffany Shaw and Malte Jansen for their critical feedback during the completion of the project. We gratefully acknowledge Clare Huang's contribution in developing and maintaining the falwa python package that has made the LWA budget analysis easier. PB also thanks George Kiladis and Camille Li for their encouragement and support during completion of the manuscript. This research was funded in part by National Science Foundation (NSF) through awards 1909522 and 2154523 and in part by European Union's Horizon 2022 research and innovation program under the Marie Sklodowska-Curie grant agreement No. 101110631.

Data availability statement. The ERA5 reanalysis data can be accessed through the ECMWF website (https://www.ecmwf.int/en/forecasts/datasets/reanalysis-datasets/era5). The LWA budget calculations can be performed using the falwa python package from `https://github.com/csyhuang/hn2016_falwa`. The wave-activity tracking algorithm and the post-processing scripts for producing manuscript figures can be accessed from `https://github.com/Pragallva/LWA-Blocking-2024`.

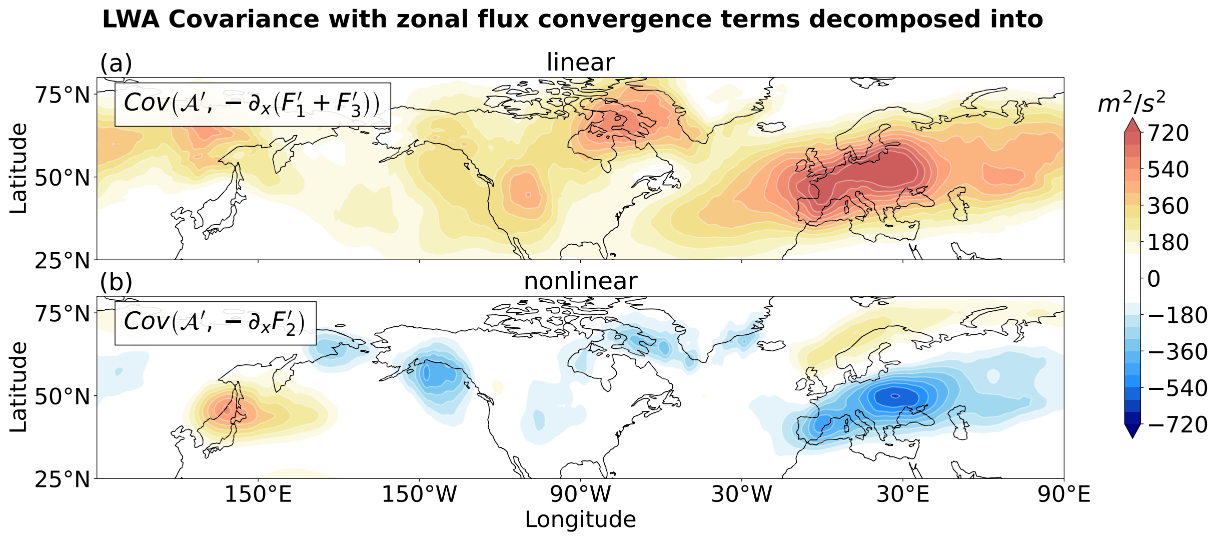

FIG. A1. Partitioning of Fig. 1b into contributions from (a) linear and (b) nonlinear fluxes using Eqs. (2b) and (3a).

APPENDIX A

Linear and nonlinear flux contributions to the LWA tendency variance budget

Corresponding to Fig. 1b, the covariance between LWA tendency and zonal flux convergence term is decomposed into linear (Fig. A1a) and nonlinear components (Fig. A1b) computed as $\mathrm{Cov}\left(\mathcal{A}', -\partial_x(F_1' + F_3')\right)$ and $\mathrm{Cov}(\mathcal{A}', -\partial_x F_2')$, respectively, where the $\mathrm{Cov}(\cdots)$ function is defined in Eq (3c). The linear covariance is predominantly positive and pronounced over the exit region of the both North Pacific and North Atlantic storm tracks, whereas the nonlinear covariance term is predominantly negative except near the east coast of Eurasia. Coincidentally, the latter also coincides with the region dominated by cyclonic blocks (see Fig. 5a). Since the convergence of the zonal fluxes promotes downstream transmission of wave packets, the positive values in Fig. A1a indicate that LWA tendency largely reflects the downstream transmission of the waves. Whereas the negative values in Fig. A1b indicate that the convergence of the nonlinear flux acts as a brake to the downstream transmission.

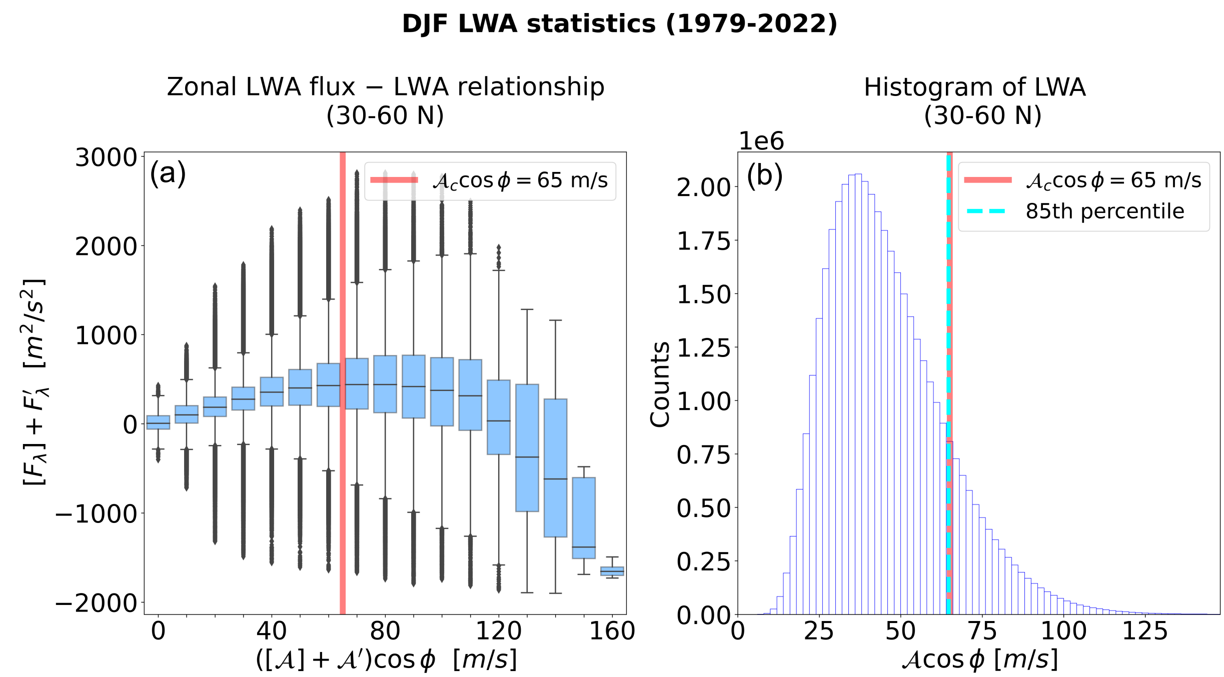

Fig. B1. Daily LWA statistics captured by (a) quartile plot showing the relationship between column-mean zonal LWA flux and column-mean LWA and (b) histogram of daily-averaged LWA values between 30-60°N. The solid red line in (a) and (b) indicates the threshold value, $\mathcal{A}_c \cos\phi = 65$ m s^{-1} and the dashed cyan line in (b) indicates 85th percentile of LWA. Data is from ERA5 reanalysis between 1979-2022 during DJF for 30-60°N latitude and all longitudes.

APPENDIX B

LWA statistical analysis

B1. Determination of LWA threshold

The threshold LWA value, $\mathcal{A}_c \cos\phi$, is determined empirically by observing the nonlinear relationship between zonal LWA-flux (F_λ) and LWA ($\mathcal{A}\cos\phi$) during DJF for all years between 1979-2022. To achieve this we make a quartile plot where F_λ values are binned over $\mathcal{A}\cos\phi$ values at an interval of 10 m s^{-1} between 30-60°N (Fig. B1a). Despite a significant spread in the wave-activity flux, the inter-quartile range of F_λ (light blue boxes in Fig. B1a) follows an approximate quadratic relationship with $\mathcal{A}\cos\phi$ as theorized by NH18 [see Eq. (6b in) the main text]. The LWA threshold is found to be approximately 65 m s^{-1} where the binned median value of

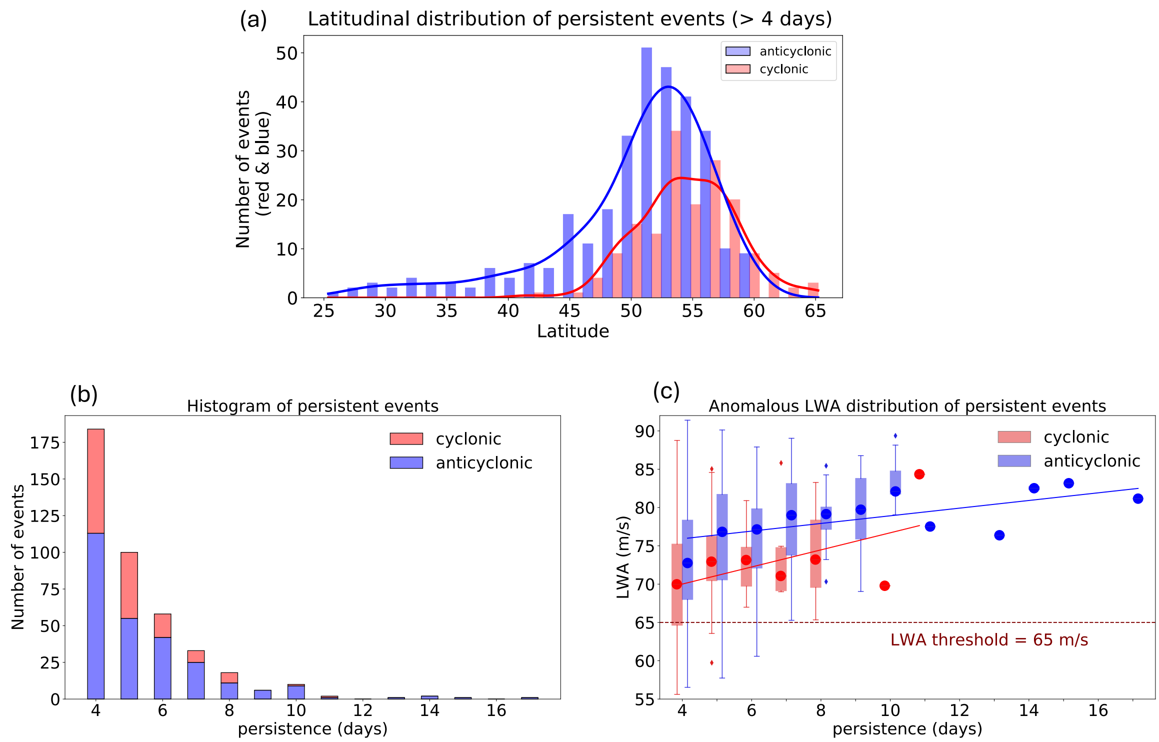

FIG. B2. Wave-activity block statistics of cyclonic and anticyclonic events captured by their (a) latitudinal distribution (b) histogram as a function of persistence and (c) quartile plot showing the relationship between LWA and persistence. The smooth curves in panel (a) are kernel density estimates of the respective histograms as computed by the python seaborn library. Data is from ERA5 reanalysis between 1979-2022 during DJF for all latitude and longitudes.

F_λ has a maxima (see red line in Fig. B1a). This chosen threshold value also happens to be the 85th percentile of total LWA as seen in Fig. B1b. Note the positive skew in the LWA distribution, which arises primarily from the nonlinearity associated with eddy-flow interaction (Valva and Nakamura 2021).

B2. Characteristics of cyclonic/anticyclonic wave-activity blocks

We summarize here some additional statistics of the persistent events identified from the tracking algorithm.

Figure B2a shows the latitudinal distribution of the wave-activity blocks for all longitudes and all persistence length. Overall, the cyclonic (red) events are fewer in number but tend to maximize poleward of the anticyclonic (blue) ones. The result is consistent with Thorncroft et al. (1993) who show that cyclonic wave breaking occurs preferentially on the poleward side of the jet and anticyclonic wave breaking occurs preferentially on the equatorward side of the jet. Figure B2b shows the histogram of blocking persistence for both cyclonic and anticyclonic events. The number of blocks decay exponentially with increase in persistence. Figure B2c shows the relationsip between LWA and persistence length for both cyclonic and anticyclonic blocks. There is a discernible trend that greater wave-activity leads to longer persistence. In addition, anticyclonic blocks tend to persist longer than the cyclonic ones. The complete latitude-longitude distribution of cyclonic and anticyclonic events is shown in Fig. 5a.

APPENDIX C

Estimation of carrying capacity

Figure C1 shows the expansion of the carrying capacity F_c [see Eq. (8)] into three contributing terms: F_{C_1}, F_{C_2} and F_{C_3}. Since we use the zonally averaged values of $u_0 + c_g^x$ and α, F_{C_1} in Fig. C1a is zonally uniform. It largely reflects the speed of the zonal jet, which maximizes in the subtropics. The zonal variation in F_C arises from the stationary LWA, $\mathcal{A}_0(\lambda, \phi)\cos\phi$ (Figs. C1b, c). In particular, the decelerating effect of $\mathcal{A}_0$ on the zonal wind appears strongly in the negative values of F_{C_3} (Fig. C1c.) As a result, the carrying capacity is large where the jet is fast and small where $\mathcal{A}_0 \cos\phi$ is large (Fig. C1d.) Blocking frequency tends to be high at locations where the carrying capacity is small (Figs. 6b, c.) .

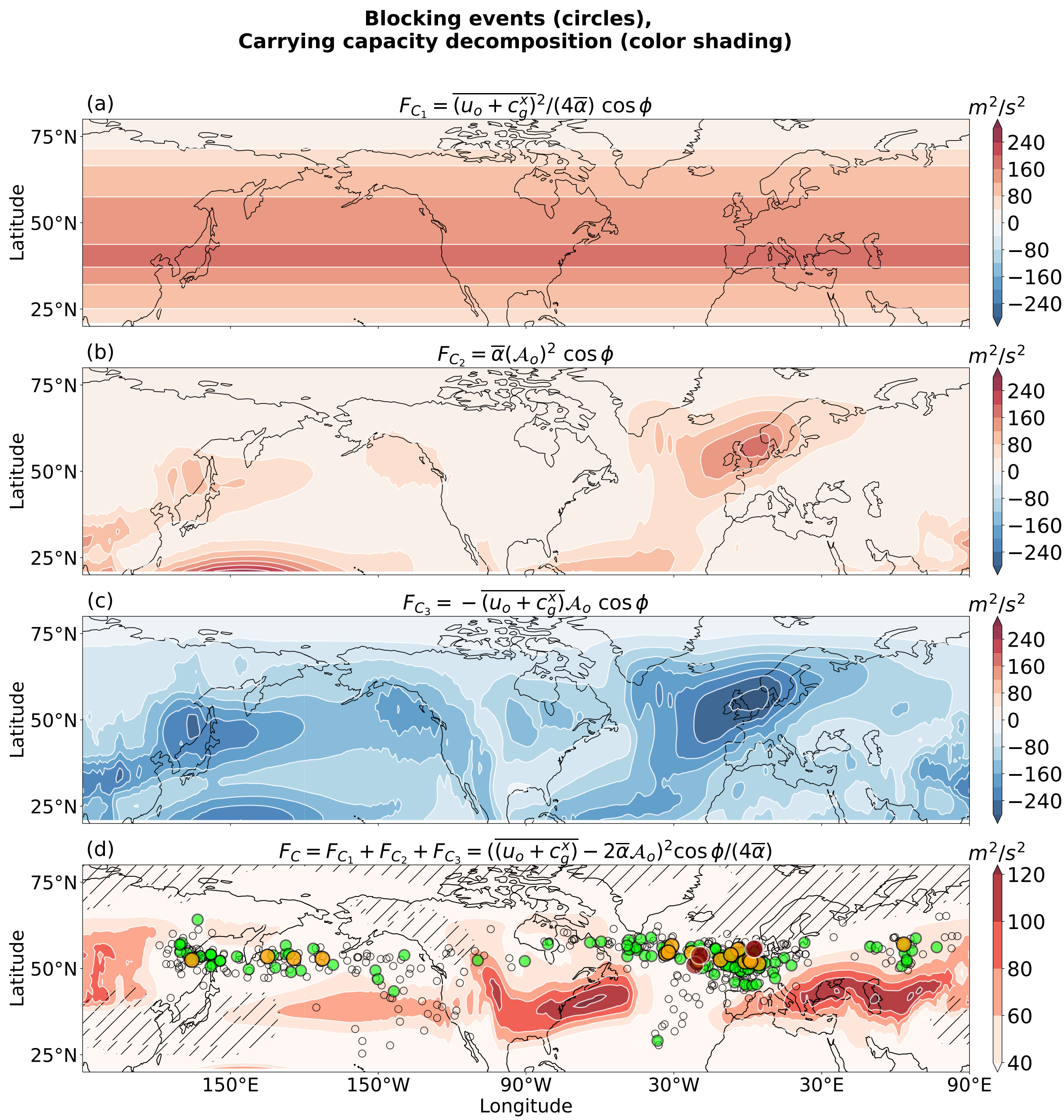

FIG. C1. Decomposition of carrying capacity into contributions from (a) $F_{C_1} = \overline{(u_0 + c_g^x)}^2 \cos\phi/(4\overline{\alpha})$, (b) $F_{C_2} = \overline{\alpha}(A_0)^2 \cos\phi$, (c) $F_{C_3} = -\overline{(u_0 + c_g^x)} A_0 \cos\phi$. (d) Sum of (a)-(c) equals the total carrying capacity in (d), which is the same as Fig. 6b. The circles show the spatial distribution of wave-activity blocks.

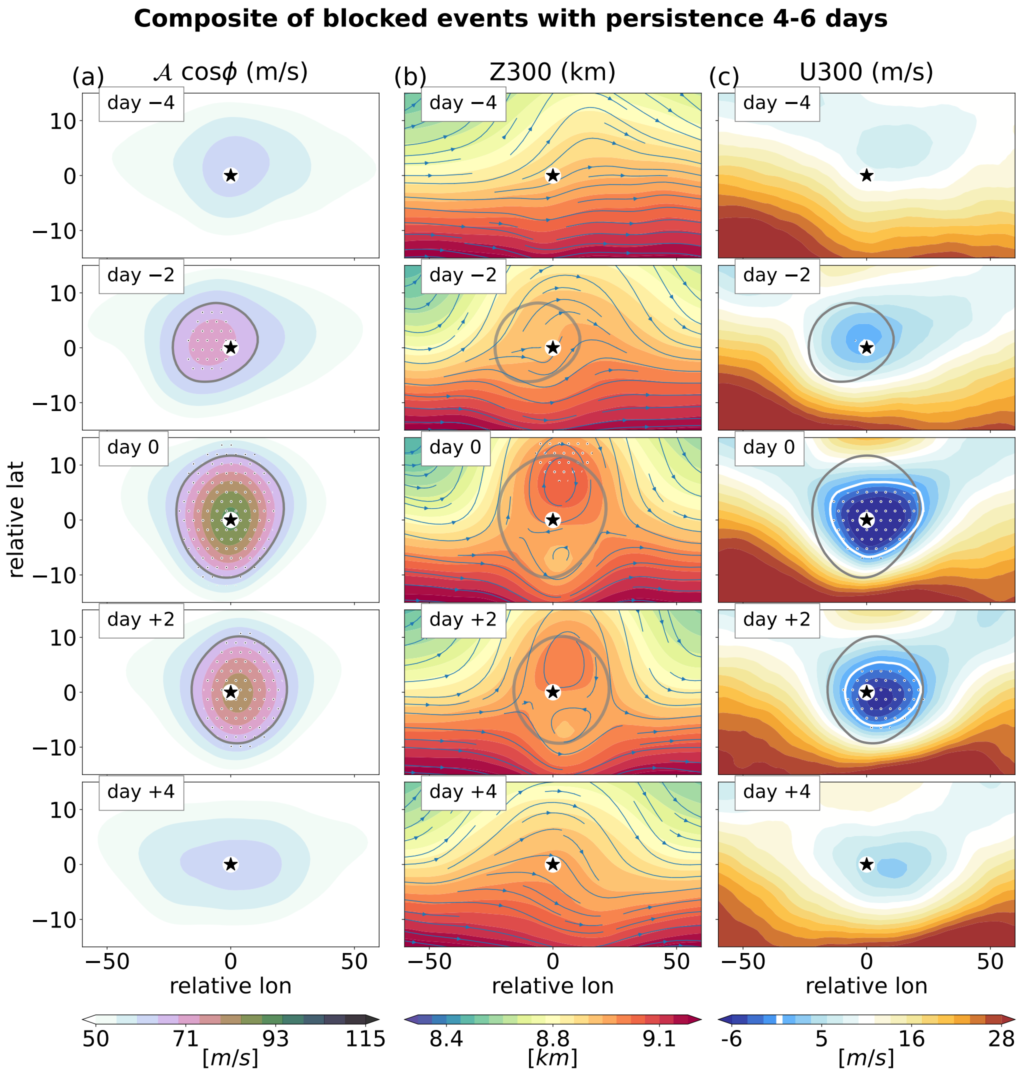

FIG. D1. Same as Fig. 4 but for the 399 events with persistence between 4-6 days. See the main text for details.

693 APPENDIX D

Composite lifecycle of short-lived events

Here we repeat the analyses of Figs. 4 and 7 for short-lived wave-activity blocks (persistence: 4-6 days).

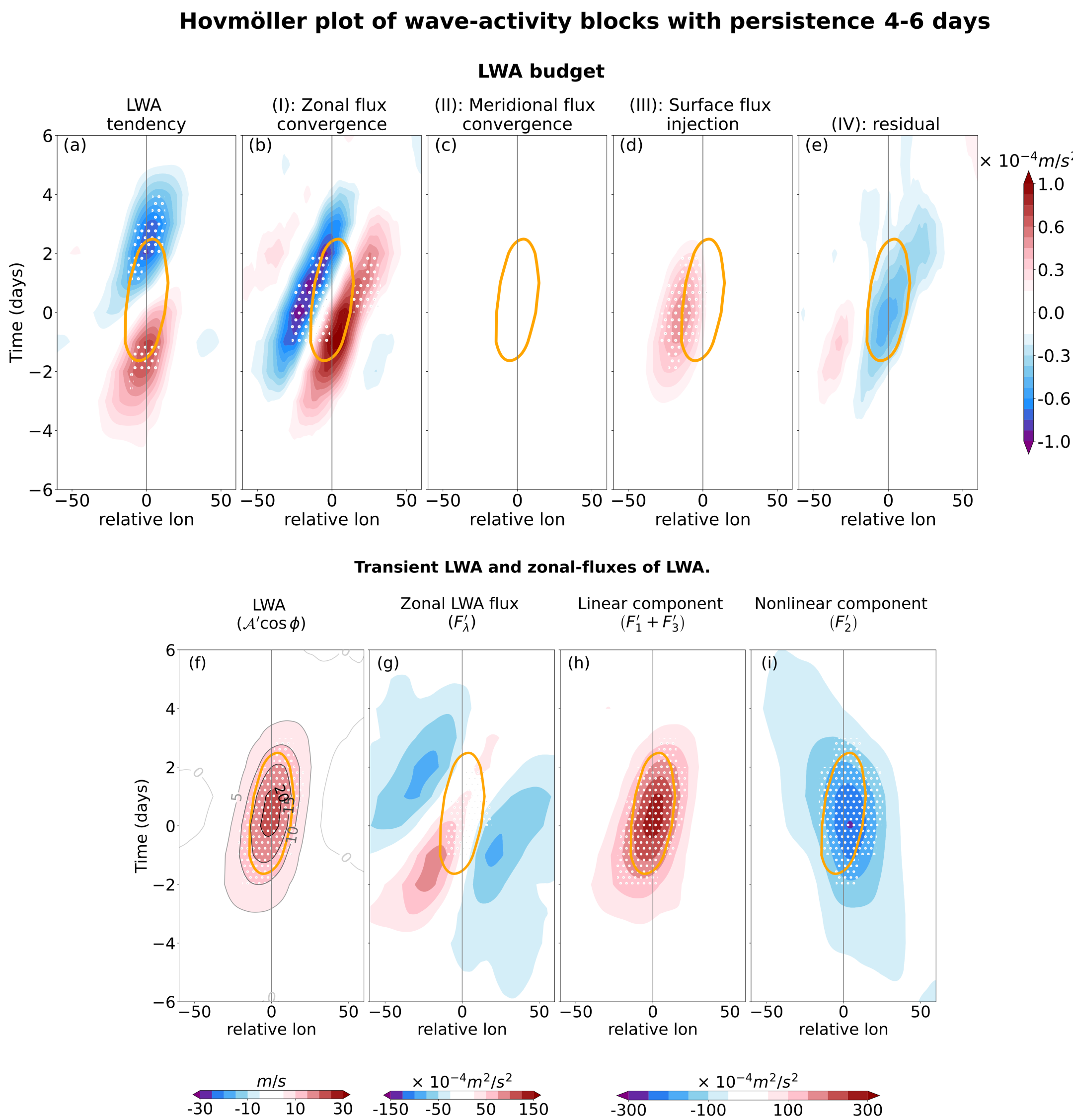

FIG. D2. Same as Fig. 7 but for the 399 events with persistence between 4-6 days. See the main text for details.

References

Altenhoff, A. M., O. Martius, M. Croci-Maspoli, C. Schwierz, and H. C. Davies, 2008: Linkage of atmospheric blocks and synoptic-scale rossby waves: a climatological analysis. *Tellus A: Dynamic Meteorology and Oceanography*, **60 (5)**, 1053–1063, https://doi.org/10.1111/j.1600-0870.2008.00354.x.

Andrews, D. G., and M. E. McIntyre, 1976: Planetary waves in horizontal and vertical shear: The generalized eliassen-palm relation and the mean zonal acceleration. *Journal of the Atmospheric Sciences*, **33**, 2031–2048, https://doi.org/10.1175/1520-0469(1976)033⟨2031:PWIHAV⟩2.0.CO;2.

Barriopedro, D., R. García-Herrera, A. R. Lupo, and E. Hernández, 2006: A Climatology of Northern Hemisphere Blocking. *Journal of Climate*, **19 (6)**, 1042–1063, https://doi.org/10.1175/JCLI3678.1.

Berggren, R., B. Bolin, and C.-G. Rossby, 1949: An aerological study of zonal motion, its perturbations and break-down. *Tellus*, **1 (2)**, 14–37, https://doi.org/10.3402/tellusa.v1i2.8501.

Butchart, N., K. Haines, and J. C. Marshall, 1989: A Theoretical and Diagnostic Study of Solitary Waves and Atmospheric Blocking. *Journal of the Atmospheric Sciences*, **46 (13)**, 2063–2078, https://doi.org/10.1175/1520-0469(1989)046⟨2063:ATADSO⟩2.0.CO;2.

Charney, J. G., 1947: The dynamics of long waves in a baroclinic westerly current. *Journal of Meteorology*, **4**, 136–162, https://doi.org/10.1175/1520-0469(1947)004⟨0136:TDOLWI⟩2.0.CO;2.

Charney, J. G., and J. G. DeVore, 1979: Multiple Flow Equilibria in the Atmosphere and Blocking. *Journal of the Atmospheric Sciences*, **36 (7)**, 1205–1216, https://doi.org/10.1175/1520-0469(1979)036⟨1205:MFEITA⟩2.0.CO;2.

Charney, J. G., and P. G. Drazin, 1961: Propagation of planetary-scale disturbances from the lower into the upper atmosphere. *Journal of Geophysical Research*, **66**, 83–109, https://doi.org/10.1029/JZ066i001p00083.

Chen, G., J. Lu, D. A. Burrows, and L. R. Leung, 2015: Local finite-amplitude wave activity as an objective diagnostic of midlatitude extreme weather. *Geophysical Research Letters*, **42 (24)**, 10,952–10,960, https://doi.org/https://doi.org/10.1002/2015GL066959.

Colucci, S. J., 2001: Planetary-Scale Preconditioning for the Onset of Blocking. *Journal of the Atmospheric Sciences*, **58 (8)**, 933–942, https://doi.org/10.1175/1520-0469(2001)058⟨0933:PSPFTO⟩2.0.CO;2.

Davini, P., and F. D'Andrea, 2016: Northern hemisphere atmospheric blocking representation in global climate models: Twenty years of improvements? *Journal of Climate*, **29 (24)**, 8823 – 8840, https://doi.org/10.1175/JCLI-D-16-0242.1.

Demirtaş, M., 2017: The large-scale environment of the european 2012 high-impact cold wave: prolonged upstream and downstream atmospheric blocking. *Weather*, **72 (10)**, 297–301, https://doi.org/10.1002/wea.3020.

Eady, E. T., 1949: Long waves and cyclone waves. *Tellus*, **1 (3)**, 33–52, https://doi.org/10.3402/tellusa.v1i3.8507.

Eliassen, A., 1952: Slow thermally or frictionally controlled meridional circulations in a circular vortex. *Astrophysica Norvegica*, **5**, 19–60.

Ghil, M., A. Groth, D. Kondrashov, and A. W. Robertson, 2019: Chapter 6 - extratropical sub-seasonal to seasonal oscillations and multiple regimes: The dynamical systems view. *Sub-Seasonal to Seasonal Prediction*, A. W. Robertson, and F. Vitart, Eds., Elsevier, 119–142, https://doi.org/https://doi.org/10.1016/B978-0-12-811714-9.00006-1.

Gollan, G., and R. J. Greatbatch, 2017: The relationship between northern hemisphere winter blocking and tropical modes of variability. *Journal of Climate*, **30 (22)**, 9321 – 9337, https://doi.org/10.1175/JCLI-D-16-0742.1.

Green, J., 1977: The weather during july 1976: Some dynamical considerations of the drought. *Weather*, **32 (4)**, 120–126.

Haines, K., and J. Marshall, 1987: Eddy-forced coherent structures as a prototype of atmospheric blocking. *Quarterly Journal of the Royal Meteorological Society*, **113 (476)**, 681–704, https://doi.org/https://doi.org/10.1002/qj.49711347613.

Held, I. M., and A. Y. Hou, 1980: Nonlinear axially symmetric circulations in a nearly inviscid atmosphere. *Journal of the Atmospheric Sciences*, **37**, 515–533, https://doi.org/10.1175/1520-0469(1980)037⟨0515:NASCIA⟩2.0.CO;2.

Henderson, S. A., E. D. Maloney, and E. A. Barnes, 2016: The influence of the Madden–Julian Oscillation on northern hemisphere winter blocking. *Journal of Climate*, **29 (12)**, 4597 – 4616, https://doi.org/10.1175/JCLI-D-15-0502.1.

Hersbach, H., and Coauthors, 2020: The era5 global reanalysis. *Quarterly Journal of the Royal Meteorological Society*, **146 (730)**, 1999–2049, https://doi.org/https://doi.org/10.1002/qj.3803.

Huang, C. S. Y., and N. Nakamura, 2016: Local Finite-Amplitude Wave Activity as a Diagnostic of Anomalous Weather Events. *Journal of the Atmospheric Sciences*, **73 (1)**, 211–229, https://doi.org/10.1175/JAS-D-15-0194.1.

Huang, C. S. Y., and N. Nakamura, 2017: Local wave activity budgets of the wintertime northern hemisphere: Implication for the pacific and atlantic storm tracks. *Geophysical Research Letters*, **44 (11)**, 5673–5682, https://doi.org/10.1002/2017GL073760.

Johnson, D. R., 1989: The forcing and maintenance of global monsoonal circulations: An isentropic analysis. *Advances in Geophysics*, **31**, 43–316, https://doi.org/10.1016/S0065-2687(08)60053-9.

Kautz, L., O. Martius, S. Pfahl, J. G. Pinto, A. M. Ramos, P. M. Sousa, and T. Woollings, 2022: Atmospheric blocking and weather extremes over the euro-atlantic sector – a review. *Weather and Climate Dynamics*, **3**, 305–336, https://doi.org/10.5194/wcd-3-305-2022.

Kuo, H.-L., 1956: Forced and free meridional circulations in the atmosphere. *Journal of Meteorology*, **13**, 561–568, https://doi.org/10.1175/1520-0469(1956)013⟨0561:FAFMCI⟩2.0.CO;2.

Legras, B., and M. Ghil, 1985: Persistent anomalies, blocking and variations in atmospheric predictability. *Journal of Atmospheric Sciences*, **42 (5)**, 433 – 471, https://doi.org/10.1175/1520-0469(1985)042⟨0433:PABAVI⟩2.0.CO;2.

Li, Z., G. Dai, and M. Mu, 2024: Effects of stratospheric warming on ural blocking events in winter. *Journal of Geophysical Research: Atmospheres*, **129 (2)**, e2023JD039 672, https://doi.org/https://doi.org/10.1029/2023JD039672.

Lighthill, M. J., and G. B. Whitham, 1955: On kinematic waves ii. a theory of traffic flow on long crowded roads. *Proceedings of the Royal Society of London. Series A. Mathematical and Physical Sciences*, **229 (1178)**, 317–345, https://doi.org/10.1098/rspa.1955.0089.

Lindzen, R. S., and J. R. Holton, 1968: A theory of the quasi-biennial oscillation. *Journal of the Atmospheric Sciences*, **25**, 1095–1107, https://doi.org/10.1175/1520-0469(1968)025⟨1095:ATOTQB⟩2.0.CO;2.

Liu, Z., and L. Wang, 2024: Enhanced occurrence of atmospheric blocking in the southern hemisphere by baroclinic annular mode. *Geophysical Research Letters*, **51 (4)**, e2023GL107 343, https://doi.org/https://doi.org/10.1029/2023GL107343.

Lucarini, V., and A. Gritsun, 2019: A new mathematical framework for atmospheric blocking events. *Climate Dynamics*, **54 (1–2)**, 575–598, https://doi.org/10.1007/s00382-019-05018-2, URL http://dx.doi.org/10.1007/s00382-019-05018-2.

Luo, D., W. Zhang, L. Zhong, and A. Dai, 2019: A Nonlinear Theory of Atmospheric Blocking: A Potential Vorticity Gradient View. *Journal of the Atmospheric Sciences*, **76 (8)**, 2399–2427, https://doi.org/10.1175/JAS-D-18-0324.1.

Luo, D.-H., 2005: Barotropic envelope rossby soliton model for block-eddy interaction. part i: Effect of topography. *Journal of the Atmospheric Sciences*, **62**, 5–21, https://doi.org/10.1175/1186.1.

Lupo, A. R., 2021: Atmospheric blocking events: a review. *Annals of the New York Academy of Sciences*, **1504**, 5–24, https://doi.org/10.1111/nyas.14557.

Mann, M. E., S. Rahmstorf, K. Kornhuber, B. A. Steinman, S. K. Miller, S. Petri, and D. Coumou, 2018: Projected changes in persistent extreme summer weather events: The role of quasi-resonant amplification. *Science Advances*, **4**, https://doi.org/10.1126/sciadv.aat3272.

Matsuno, T., 1971: A dynamical model of the stratospheric sudden warming. *Journal of the Atmospheric Sciences*, **28**, 1479–1494, https://doi.org/10.1175/1520-0469(1971)028⟨1479:ADMOTS⟩2.0.CO;2.

McWilliams, J. C., 1980: An application of equivalent modons to atmospheric blocking. *Dynamics of Atmospheres and Oceans*, **5 (1)**, 43 – 66, https://doi.org/https://doi.org/10.1016/0377-0265(80)90010-X.

Mullen, S. L., 1987: Transient Eddy Forcing of Blocking Flows. *Journal of the Atmospheric Sciences*, **44 (1)**, 3–22, https://doi.org/10.1175/1520-0469(1987)044⟨0003:TEFOBF⟩2.0.CO;2.

Nakamura, H., M. Nakamura, and J. L. Anderson, 1997: The Role of High- and Low-Frequency Dynamics in Blocking Formation. *Monthly Weather Review*, **125 (9)**, 2074–2093, https://doi.org/10.1175/1520-0493(1997)125⟨2074:TROHAL⟩2.0.CO;2.

Nakamura, N., 2024: Large-scale eddy-mean flow interaction in the earth's extratropical atmosphere. *Annual Review of Fluid Mechanics*, **56 (Volume 56, 2024)**, 349–377, https://doi.org/https://doi.org/10.1146/annurev-fluid-121021-035602.

Nakamura, N., and C. S. Y. Huang, 2017: Local wave activity and the onset of blocking along a potential vorticity front. *Journal of the Atmospheric Sciences*, **74 (7)**, 2341–2362, https://doi.org/10.1175/JAS-D-17-0029.1.

Nakamura, N., and C. S. Y. Huang, 2018: Atmospheric blocking as a traffic jam in the jet stream. *Science*, **361 (6397)**, 42–47, https://doi.org/10.1126/science.aat0721.

Narinesingh, V., J. F. Booth, S. K. Clark, and Y. Ming, 2020: Atmospheric blocking in an aquaplanet and the impact of orography. *Weather and Climate Dynamics*, **1 (2)**, 293–311, https://doi.org/10.5194/wcd-1-293-2020.

Neal, E., C. S. Y. Huang, and N. Nakamura, 2022: The 2021 pacific northwest heat wave and associated blocking: Meteorology and the role of an upstream cyclone as a diabatic source of wave activity. *Geophysical Research Letters*, **49**, e2021GL097 699, https://doi.org/10.1029/2021GL097699.

Paradise, A., C. B. Rocha, P. Barpanda, and N. Nakamura, 2019: Blocking Statistics in a Varying Climate: Lessons from a "Traffic Jam" Model with Pseudostochastic Forcing. *Journal of the Atmospheric Sciences*, **76 (10)**, 3013–3027, https://doi.org/10.1175/JAS-D-19-0095.1.

Pelly, J. L., and B. J. Hoskins, 2003: A New Perspective on Blocking. *Journal of the Atmospheric Sciences*, **60 (5)**, 743–755, https://doi.org/10.1175/1520-0469(2003)060⟨0743:ANPOB⟩2.0.CO;2.

Petoukhov, V., S. Rahmstorf, S. Petri, and H. J. Schellnhuber, 2013: Quasiresonant amplification of planetary waves and recent northern hemisphere weather extremes. *Proceedings of National Academy of Sciences, USA*, **110**, 5336–5341, https://doi.org/10.1073/pnas.1222000110.

Pfahl, S., C. Schwierz, M. Croci-Maspoli, C. M. Grams, and H. Wernli, 2015: Importance of latent heat release in ascending air streams for atmospheric blocking. *Nature Geoscience*, **8 (8)**, 610–614.

Phillips, N. A., 1951: A simple three-dimensional model for the study of large-scale extratropical flow patterns. *Journal of Meteorology*, **8**, 381–394, https://doi.org/10.1175/1520-0469(1951)008⟨0381:ASTDMF⟩2.0.CO;2.

Plumb, R. A., 1977: The interaction of two internal waves with the mean flow: Implications for the theory of the quasi-biennial oscillation. *Journal of the Atmospheric Sciences*, **34**, 1847–1858, https://doi.org/10.1175/1520-0469(1977)034⟨1847:TIOTIW⟩2.0.CO;2.

Plumb, R. A., 1986: Three-dimensional propagation of transient quasi-geostrophic eddies and its relationship with the eddy forcing of the time—mean flow. *Journal of Atmospheric Sciences*, **43 (16)**, 1657 – 1678, https://doi.org/https://doi.org/10.1175/1520-0469(1986)043⟨1657:TDPOTQ⟩2.0.CO;2.

Polster, C., and V. Wirth, 2023: The onset of a blocking event as a “traffic jam”: Characterization with ensemble sensitivity analysis. *Journal of the Atmospheric Sciences*, **80 (7)**, 1681 – 1699, https://doi.org/10.1175/JAS-D-21-0312.1.

Rex, D. F., 1950: Blocking action in the middle troposphere and its effect upon regional climate. *Tellus*, **2 (4)**, 275–301, https://doi.org/10.3402/tellusa.v2i4.8603.

Richards, P. I., 1956: Shock waves on the highway. *Operations Research*, **4 (1)**, 42–51, https://doi.org/10.1287/opre.4.1.42.

Rodwell, M. J., and Coauthors, 2013: Characteristics of occasional poor medium-range weather forecasts for europe. *Bulletin of the American Meteorological Society*, **94**, 1393–1405, https://doi.org/10.1175/BAMS-D-12-00099.1.

Scaife, A. A., T. Woollings, J. Knight, G. Martin, and T. Hinton, 2010: Atmospheric Blocking and Mean Biases in Climate Models. *Journal of Climate*, **23 (23)**, 6143–6152, https://doi.org/10.1175/2010JCLI3728.1.

Shutts, G., 1983: The propagation of eddies in diffluent jetstreams: Eddy vorticity forcing of 'blocking' flow fields. *Quarterly Journal of the Royal Meteorological Society*, **109 (462)**, 737–761.

Steinfeld, D., M. Boettcher, R. Forbes, and S. Pfahl, 2020: The sensitivity of atmospheric blocking to upstream latent heating – numerical experiments. *Weather and Climate Dynamics*, **1 (2)**, 405–426, https://doi.org/10.5194/wcd-1-405-2020.

Steinfeld, D., and S. Pfahl, 2019: The role of latent heating in atmospheric blocking dynamics: A global climatology. *Climate Dynamics*, **53**, 6159–6180, https://doi.org/10.1007/s00382-019-04919-6.

Swanson, K. L., 2000: Stationary Wave Accumulation and the Generation of Low-Frequency Variability on Zonally Varying Flows. *Journal of the Atmospheric Sciences*, **57 (14)**, 2262–2280, https://doi.org/10.1175/1520-0469(2000)057⟨2262:SWAATG⟩2.0.CO;2.

Thorncroft, C. D., B. J. Hoskins, and M. E. McIntyre, 1993: Two paradigms of baroclinic-wave life-cycle behaviour. *Quarterly Journal of the Royal Meteorological Society*, **119 (509)**, 17–55, https://doi.org/https://doi.org/10.1002/qj.49711950903.

Tilly, D. E., A. R. Lupo, C. J. Melick, and P. S. Market, 2008: Calculated height tendencies in two southern hemisphere blocking and cyclone events: The contribution of diabatic heating to block intensification. *Monthly Weather Review*, **136 (9)**, 3568 – 3578, https://doi.org/10.1175/2008MWR2374.1.

Trenberth, K. E., 1986: The signature of a blocking episode on the general circulation in the southern hemisphere. *Journal of the Atmospheric Sciences*, **43**, 2061–2069, https://doi.org/10.1175/1520-0469(1986)043⟨2061:TSOABE⟩2.0.CO;2.

Tung, K. K., and R. S. Lindzen, 1979: A Theory of Stationary Long Waves. Part I: A Simple Theory of Blocking. *Monthly Weather Review*, **107 (6)**, 714–734, https://doi.org/10.1175/1520-0493(1979)107⟨0714:ATOSLW⟩2.0.CO;2.

Valva, C., and N. Nakamura, 2021: What controls the probability distribution of local wave activity in the midlatitudes? *Journal of Geophysical Research – Atmospheres*, **126**, e2020JD034 501, https://doi.org/10.1029/2020JD034501.

Vial, J., and T. J. Osborn, 2012: Assessment of atmosphere-ocean general circulation model simulations of winter northern hemisphere atmospheric blocking. *Clim Dyn*, **39 (1)**, 95–112, https://doi.org/10.1007/s00382-011-1177-z.

Wirth, V., and C. Polster, 2022: The problem of diagnosing jet waveguidability in the presence of large-amplitude eddies. *Journal of the Atmospheric Sciences*, **78**, 3137–3151, https://doi.org/10.1175/JAS-D-20-0292.1.

Woollings, T., A. Charlton-Perez, S. Ineson, A. G. Marshall, and G. Masato, 2010a: Associations between stratospheric variability and tropospheric blocking. *Journal of Geophysical Research: Atmospheres*, **115 (D6)**, https://doi.org/https://doi.org/10.1029/2009JD012742.

Woollings, T., A. Hannachi, and B. Hoskins, 2010b: Variability of the north atlantic eddy-driven jet stream. *Quarterly Journal of the Royal Meteorological Society*, **136 (649)**, 856–868, https://doi.org/10.1002/qj.625.

Woollings, T., B. Hoskins, M. Blackburn, and P. Berrisford, 2008: A New Rossby Wave–Breaking Interpretation of the North Atlantic Oscillation. *Journal of the Atmospheric Sciences*, **65 (2)**, 609–626, https://doi.org/10.1175/2007JAS2347.1.

Woollings, T., and Coauthors, 2018: Blocking and its response to climate change. *Current climate change reports*, **4 (3)**, 287–300.

Yamazaki, A., and H. Itoh, 2013: Vortex–vortex interactions for the maintenance of blocking. part i: The selective absorption mechanism and a case study. *Journal of the Atmospheric Sciences*, **70**, 725–742, https://doi.org/10.1175/JAS-D-11-0295.1.